Mon. Not. R. Astron. Soc. **000**, 1–19 (2015) Printed 10 March 2015 (MN LATEX style file v2.2)

Modelling the supernova-driven ISM in different environments

A. Gatto,[1⋆] S. Walch,[2,1] M.-M. Mac Low,[3] T. Naab,[1] P. Girichidis,[1] S. C. O. Glover,[4] R. Wünsch,[5] R. S. Klessen,[4,6,7] P. C. Clark,[8,4] C. Baczynski,[4,3] T. Peters,[9,1] J. P. Ostriker,[10,11] J. C. Ibáñez-Mejía[3,4] and S. Haid[2]

[1] *Max-Planck-Institut für Astrophysik, Karl-Schwarzschild-Strasse 1, D-85748 Garching, Germany*
[2] *Physikalisches Institut, Universität Köln, Zülpicher Strasse 77, D-50937 Köln, Germany*
[3] *Department of Astrophysics, American Museum of Natural History, 79th Street at Central Park West, New York, NY 10024, USA*
[4] *Universität Heidelberg, Zentrum für Astronomie, Institut für Theoretische Astrophysik, Albert-Ueberle-Str. 2, D-69120 Heidelberg, Germany*
[5] *Astronomický Ústav, Akademie věd Česk Republiky, Boční II 1401, C-14131 Praha, Czech Republic*
[6] *Department of Astronomy and Astrophysics, University of California, 1156 High Street, Santa Cruz, CA 95064, USA*
[7] *Kavli Institute for Particle Astrophysics and Cosmology, Stanford University, SLAC Nat. Acc. Lab., Menlo Park, CA 94025, USA*
[8] *School of Physics and Astronomy, Cardiff University, 5 The Parade, Cardiff CF24 3AA, UK*
[9] *Institut für Computergestützte Wissenschaften, Universität Zürich, Winterthurerstrasse 190, CH-8057 Zürich, Switzerland*
[10] *Department of Astrophysical Sciences, Princeton University, 4 Ivy Ln, Princeton, NJ 08544, USA*
[11] *Department of Astronomy, Columbia University, 550 West 120th Street, New York, NY 10027, USA*

arXiv:1411.0009v2 [astro-ph.GA] 8 Mar 2015

Accepted 2015 January 28. Received 2015 January 21; in original form 2014 October 31

ABSTRACT

We use hydrodynamical simulations in a $(256\ \mathrm{pc})^3$ periodic box to model the impact of supernova (SN) explosions on the multi-phase interstellar medium (ISM) for initial densities $n = 0.5$–$30\ \mathrm{cm}^{-3}$ and SN rates 1–720 Myr^{-1}. We include radiative cooling, diffuse heating, and the formation of molecular gas using a chemical network. The SNe explode either at random positions, at density peaks, or both. We further present a model combining thermal energy for resolved and momentum input for unresolved SNe. Random driving at high SN rates results in hot gas ($T \gtrsim 10^6$ K) filling $> 90\%$ of the volume. This gas reaches high pressures ($10^4 < P/k_\mathrm{B} < 10^7\ \mathrm{K\ cm}^{-3}$) due to the combination of SN explosions in the hot, low density medium and confinement in the periodic box. These pressures move the gas from a two-phase equilibrium to the single-phase, cold branch of the cooling curve. The molecular hydrogen dominates the mass ($> 50\%$), residing in small, dense clumps. Such a model might resemble the dense ISM in high-redshift galaxies. Peak driving results in huge radiative losses, producing a filamentary ISM with virtually no hot gas, and a small molecular hydrogen mass fraction ($\ll 1\%$). Varying the ratio of peak to random SNe yields ISM properties in between the two extremes, with a sharp transition for equal contributions. The velocity dispersion in HI remains $\lesssim 10\,\mathrm{km\,s}^{-1}$ in all cases. For peak driving the velocity dispersion in H_α can be as high as $70\,\mathrm{km\,s}^{-1}$ due to the contribution from young, embedded SN remnants.

Key words: galaxies: evolution – ISM: evolution – ISM: structure – ISM: kinematics and dynamics – ISM: supernova remnants – methods: numerical

1 INTRODUCTION

Supernova (SN) explosions are an important component for shaping the interstellar medium (ISM). In particular, they produce its hottest phase, with temperature $\mathrm{T} \gtrsim 10^6$ K (Cox & Smith 1974; McKee & Ostriker 1977). In the Milky Way, this hot phase fills from 20% to 80% of the volume with increasing height above the disc (Ferrière 2001; Kalberla & Dedes 2008). SNe also drive turbulent motions in the ISM gas (Norman & Ferrara 1996; Joung & Mac Low 2006; de Avillez & Breitschwerdt 2007; Gent et al. 2013), although their relative importance with respect to other driving mechanisms has yet to be fully determined (see, e.g., Mestel & Spitzer 1956; Sellwood & Balbus 1999; Kritsuk & Norman 2002; Wada et al. 2002; Tamburro et al. 2009; Klessen & Hennebelle 2010).

⋆ e-mail: andreag@mpa-garching.mpg.de

© 2015 RAS

Supersonic turbulent motions in warm and cold gas, observed in emission from HI, have been found in many local and extra-galactic environments, with a typical one-dimensional velocity dispersion of $\sigma \simeq 10\,\mathrm{km\,s^{-1}}$ (e.g. Heiles & Troland 2003; Petric & Rupen 2007; Tamburro et al. 2009). Similar velocity dispersions for molecular gas have been found from CO emission lines at galactic scales (Caldú-Primo et al. 2013), with a decrease to a few kilometers per second when observing small, isolated molecular structures (Larson 1981) and a transition to transonic motions at the scale of dense cores (~ 0.1 pc; Goodman et al. 1998). Globally, these random motions could provide an effective turbulent pressure (Ostriker et al. 2010) and help to regulate star formation (Mac Low & Klessen 2004; Elmegreen & Scalo 2004).

SNe are able to heat up the ISM, influencing its pressure and dispersing the gas locally (e.g. McKee & Ostriker 1977; Mac Low et al. 2005; Joung & Mac Low 2006; de Avillez & Breitschwerdt 2004, 2007; Joung et al. 2009). However, they could also sweep up the medium, causing colliding flows that may trigger new molecular cloud and star formation events (Elmegreen & Lada 1977; Heitsch et al. 2006; Vázquez-Semadeni et al. 2006; Banerjee et al. 2009; Heitsch et al. 2011).

Type II SN progenitors are massive OB stars with typically low space velocities of ≈ 15 km s^{-1} (Stone 1991). Due to these velocities, they can only travel tens to hundreds of parsecs away from their birthplaces during their lifetimes. However, 10–30% of O stars and 5–10% of B stars in the Galaxy are runaway stars, which have large velocities (from 30 to a few hundred $\mathrm{km\,s^{-1}}$; Blaauw 1961; Gies 1987; Gies & Bolton 1986; Stone 1991) and are therefore found far from associations (from several hundred parsecs to a kiloparsec away from their birthplaces). Runaway stars are produced by dynamical ejection by means of gravitational scattering (Gies & Bolton 1986; Fujii & Portegies Zwart 2011; Perets & Šubr 2012), by massive binary systems where one of the two stars explodes as a SN, which leads to the ejection of the unbound companion (Blaauw 1961; Portegies Zwart 2000; Eldridge et al. 2011), or both mechanisms (Pflamm-Altenburg & Kroupa 2010).

Runaway massive stars typically explode in the diffuse ISM, i.e. in random positions, which are not correlated with the dense molecular clouds within which massive star formation takes place. This also applies to Type Ia SNe, which add an additional random component of SN explosions due to the long lifetimes of their progenitors.

A high fraction of massive stars (70–90 %; Lada & Lada 2003) also form in clusters and associations, rather than in isolation. Despite being initially embedded in high density environments, the high degree of clustering and multiplicity of Type II SN progenitors causes the majority of SN explosions to happen within low density gas that has previously been processed by the combined effect of stellar winds (Tenorio-Tagle et al. 1990, 1991; Brighenti & D'Ercole 1994; Rogers & Pittard 2013) and HII regions (Gritschneder et al. 2009; Walch et al. 2012, 2013; Dale et al. 2014), as well as earlier SNe in superbubbles (McCray & Kafatos 1987; Mac Low & McCray 1988; Tenorio-Tagle & Bodenheimer 1988). However, there is evidence that SNe are also interacting with the dense gas. In the inner Galaxy, around 15% of identified SN remnants show clear signs of interaction with molecular gas, including water maser emission (Hewitt & Yusef-Zadeh 2009) and TeV γ-ray emission (Fukui et al. 2003). Overall, SNe that explode in any of the above low density environments can be approximated by explosions at random positions in an ISM with a significant volume filling fraction (VFF) of hot gas. The remaining fraction of SNe interacting with dense gas can be modelled via explosions within the densest gas parcels (Walch & Naab 2014).

Several studies of the SN-driven ISM have been carried out in the past, assuming clustered, random or density peak positions for the explosions. For instance, de Avillez & Breitschwerdt (2004) studied a representative piece of a stratified galactic disc, shaped by SNe going off at fixed rate and mostly placed in regions with highest density. Joung & Mac Low (2006) performed similar simulations but chose random positions for their explosion locations. In a recent paper, Hennebelle & Iffrig (2014) perform magneto-hydrodynamical simulations of a stratified Galactic disc modelling star formation via star cluster sink particles. They show that SN explosions correlated in space and time with the particles' position and accretion can significantly inhibit further star formation. Similar conclusions have been drawn in Iffrig & Hennebelle (2014). A massive star exploding outside of the dense gas has a limited effect with respect to the case where the explosion is located within the cloud. In the latter case, a higher fraction of momentum is transferred to the cold gas and up to half of the cloud's mass can be removed by the SN. Despite the number of previous works investigating the effect of SNe on both stratified (e.g. Shetty & Ostriker 2012; Hill et al. 2012; Gent et al. 2013; Kim et al. 2013) and unstratified ISM (see, e.g., Balsara et al. 2004; Kim 2004; Slyz et al. 2005; Mac Low et al. 2005; Dib et al. 2006, for modelling in periodic boxes), a systematic study is missing of the impact of different assumed SN positions, as well as the consequences of varying the SN rate with the gas density.

In this paper, we model the turbulent, multi-phase ISM in regions of different mean density over a timescale of ~ 100 Myr with fixed (Type II) SN rates, which are informed by the Kennicutt-Schmidt (KS) relation (Schmidt 1959; Kennicutt 1998). We include a chemical network allowing us to partially model the effects of non-equilibrium chemistry in the warm gas, as well as the formation of H_2 and CO including dust and self-shielding. We focus on three different scientific questions:

(i) Given a certain initial gas density, how do the properties of the ISM depend on the assumed SN rate?

(ii) What are the differences between a medium shaped by SNe placed randomly or at density peaks?

(iii) How does the ISM change as a function of the ratio between SNe that explode randomly or at density peaks?

The paper is organised as follows: in section 2 we describe our model and runs. In section 3 we show our results. Finally, we present our conclusions in section 4.

2 NUMERICAL METHOD, PARAMETERS AND RUNS

2.1 Simulation method

We use the Eulerian, adaptive mesh refinement, hydrodynamic code FLASH 4 (Fryxell et al. 2000; Dubey et al. 2008; Dubey et al. 2013) to model the SN-driven ISM in three-dimensional (3D) simulations. We use the directionally split, Bouchut HLL5R solver (Bouchut et al. 2007; Waagan 2009; Bouchut et al. 2010) to simulate a volume of $(256\ \mathrm{pc})^3$ with periodic boundary conditions. For the majority of the simulations the resolution is fixed to 128^3 cells ($\Delta x = 2$ pc), but we run a few setups at higher resolution (see section 3.8). In different simulations, we change the initial total number density of the box from $n_\mathrm{i} = 0.5\ \mathrm{cm}^{-3}$ to $n_\mathrm{i} = 30\ \mathrm{cm}^{-3}$ (see Table 1) and the initial temperature is 6000 K.

2.2 Gas cooling and chemistry

We include a chemical network to treat radiative cooling and diffuse heating as well as molecule formation. In the cold and warm gas, the main contributions to the cooling rate come from Lyman-α cooling, H_2 ro-vibrational line cooling, fine structure emission from CII and O, and rotational line emission from CO. These processes are modelled using the prescription developed in Glover & Mac Low (2007a,b), Glover et al. (2010) and Glover & Clark (2012). The chemical network therefore follows the abundances of five key chemical species: HI, HII, H_2, CII and CO. For the formation of molecular hydrogen and CO, the effects of dust shielding and molecular (self-)shielding are included using the TREECOL algorithm of Clark et al. (2012). Full details of the implementation of these processes within FLASH 4 are described in Walch et al. (2014) and Wünsch et al. (in prep.).

In hot gas, the excitation of helium and of partially ionised metals (e.g. OVI) becomes important. The contribution to the cooling rate from these processes is computed from the cooling rates of Gnat & Ferland (2012), which assume that the atoms and ions are in collisional ionisation equilibrium. However, we explicitly follow the hydrogen ionisation state since non-equilibrium effects are noticeable for gas at temperatures around 10^4 K (see, e.g., Walch et al. 2011; Micic et al. 2013).

Diffuse heating from the photoelectric effect, cosmic rays, and X-rays is included following the prescriptions of Glover et al. (2010) and Glover & Clark (2012). We assume a constant radiation field where the photo-ionisation from point sources is neglected. The far-UV interstellar radiation field is $G_0 = 1.7$ (Habing 1968; Draine 1978), while the cosmic ray ionisation rate of HI is $\zeta = 3 \times 10^{-17}\ \mathrm{s}^{-1}$. For the X-ray ionisation and heating rates we use the values of Wolfire et al. (1995). The (constant) dust-to-gas mass ratio is set to 10^{-2}. We assume standard solar ratio of hydrogen to helium and solar metallicity with abundances $x_\mathrm{O,Si} = 3.16 \times 10^{-4}$, $x_\mathrm{SiII} = 1.5 \times 10^{-5}$ (Sembach et al. 2000), and $x_\mathrm{C,tot} = 1.41 \times 10^{-4}$. At $t = 0$ the gas has an ionisation fraction of 0.1.

n_i (cm^{-3})	Σ_gas ($\mathrm{M}_\odot\ \mathrm{pc}^{-2}$)	$\dot{N}_\mathrm{SN,-}$ (Myr^{-1})	$\dot{N}_\mathrm{SN,KS}$ (Myr^{-1})	$\dot{N}_\mathrm{SN,+}$ (Myr^{-1})
0.5	4.1	-	1.2	-
1	8.1	1.5	3	6
3	24.3	7	14	28
10	81.2	38.5	77	154
30	243	180	360	720

Table 1. Parameters of the simulations. Column 1 gives the mean volume density n_i and column 2 gives the corresponding gas surface density. In column 3 to 5 we list the simulated SN rates, where $\dot{N}_\mathrm{SN,KS}$ is derived from eq. (2).

2.3 Initial turbulent stirring

At first, the gas is stirred with an Ornstein-Uhlenbeck random process (Eswaran & Pope 1988) with dimensionless wavenumbers $k = 1$–2, where $k = 1$ corresponds to the box side, L. The phase turnover time is $t_\mathrm{drive} = 25$ Myr, which corresponds to one crossing time for the warm gas. We distribute the turbulent energy onto solenoidal and compressive modes, using a 2:1 ratio. At every time step the total energy input is adjusted such that we obtain a global, mass-weighted, 3D root-mean-square (rms) velocity that is roughly constant at $v_\mathrm{3D,rms} = 10\,\mathrm{km\,s}^{-1}$. We stir the gas for one crossing time (25 Myr) in order to generate a turbulent two-phase medium before the onset of SN driving (see also Walch et al. 2011).

2.4 Supernova driving

After 25 Myr, the artificial turbulent driving is stopped. Instead, we initialise SN explosions at a fixed rate, which we adjust to the mean box mass density ρ_i. We compute the gas surface density of the box as $\Sigma_\mathrm{gas} = \rho_\mathrm{i} L$. The Kennicutt-Schmidt relation (Kennicutt 1998):

$$\frac{\Sigma_\mathrm{SFR}}{\mathrm{M}_\odot \mathrm{yr}^{-1}\mathrm{kpc}^{-2}} = 2.5 \times 10^{-4} \left(\frac{\Sigma_\mathrm{gas}}{\mathrm{M}_\odot \mathrm{pc}^{-2}}\right)^{1.4}, \qquad (1)$$

relates the total gas surface density $\Sigma_\mathrm{gas} = \Sigma_{\mathrm{HI+H_2}}$ to a typical star formation rate (SFR) surface density. For a conventional stellar initial mass function (e.g. Salpeter 1955), approximately 100 $\mathrm{M}_\odot$ of gas that collapses into stars produces on average only one massive star, which will explode as a SN Type II at the end of its lifetime. Hence, we only consider Type II SNe and neglect the additional contribution from Type Ia SNe, which is $\sim 15\%$ of the total SN rate in the Galaxy (Tammann et al. 1994). With this information we compute the SN rate, $\dot{N}_\mathrm{SN,KS}$, for every n_i as

$$\frac{\dot{N}_\mathrm{SN,KS}}{\mathrm{Myr}} = \frac{\Sigma_\mathrm{SFR}}{\mathrm{M}_\odot \mathrm{Myr}^{-1}\mathrm{pc}^{-2}} \times 10^{-2} \frac{L^2}{\mathrm{pc}^2}\ . \qquad (2)$$

The SN rate derived in this way is afflicted with uncertainties of at least a factor of 2. For this reason we vary the SN rate by a factor of 2 for a number of initial densities. We list $\dot{N}_\mathrm{SN}$ for each density in Table 1.

2.5 Supernova energy and momentum input

For the majority of our simulations, each SN injects $E_\mathrm{SN} = 10^{51}$ erg of thermal energy into the ISM. We distribute this

energy within a sphere with radius $R_{\rm inj}$. The radius of the injection region is adjusted such that it encloses 10^3 $\rm M_\odot$ of gas, but we require $R_{\rm inj}$ to be resolved with a minimum of 4 cells:

$$R_{\rm inj} = \begin{cases} \left(\frac{3}{4\pi}\frac{10^3 \rm M_\odot}{\overline{\rho}}\right)^{\frac{1}{3}} & \text{if } R_{\rm inj} \geqslant 4\Delta x \\ 4\Delta x & \text{if } R_{\rm inj} < 4\Delta x \ , \end{cases} \quad (3)$$

where $\overline{\rho}$ is the mean density within the injection region. Here, we present a SN model that combines the injection of thermal energy and momentum and which adjusts to the local environment of each SN explosion (see section 3.7).

2.5.1 Thermal energy input

If the SNe are resolved, we inject all of the SN energy in the form of thermal energy. Typically, the gas within $R_{\rm inj}$ is then heated up to $\approx 10^6$–10^7 K, which corresponds to a local sound speed $c_{\rm s}$ of a few hundred km $\rm s^{-1}$. The associated pressure increase causes a Sedov-Taylor blast wave to expand into the ambient ISM. We decrease the time-step according to a modified Courant-Friedrichs-Lewy (CFL) condition to capture the dynamics of the blast wave:

$$\Delta t = C_{\rm CFL}\frac{\Delta x}{\max(|v| + c_{\rm s})} \ . \quad (4)$$

2.5.2 Momentum input

In case of high densities within the injection region, the Sedov-Taylor phase of the SN remnant is unresolved. The mass within the injection region is high ($M_{\rm inj}$ > few $\times$ 10^3 $\rm M_\odot$), and therefore the thermal energy input would result in an effective temperature below 10^6 K:

$$T_{\rm i,SN} = (\gamma - 1)\frac{E_{\rm SN}}{M_{\rm inj}}\frac{\mu m_{\rm p}}{k_{\rm B}} \ < 10^6 \ {\rm K} \ , \quad (5)$$

where γ is the polytropic index, μ the mean molecular weight, $m_{\rm p}$ the proton mass and $k_{\rm B}$ the Boltzmann constant.

The cooling rate is a non-linear function of the gas temperature. At $T < 10^6$ K the injected energy is almost instantaneously lost due to strong radiative cooling. The employment of a limited mass and/or spatial resolution may then lead to over-cooling, which is a well-known problem in galaxy simulations (e.g. Stinson et al. 2006; Creasey et al. 2011; Gatto et al. 2013). Many different solutions have been put forward to address the problem of unresolved SNe: switching off cooling for a certain time after the explosion (e.g. Thacker & Couchman 2000); clustering of massive stars to develop superbubbles (e.g. Shull & Saken 1995; Krause et al. 2013; Keller et al. 2014; Sharma et al. 2014); or momentum rather than energy input (e.g. Kim et al. 2011; Shetty & Ostriker 2012). Of course one could just increase the resolution (see section 3.8).

We choose a momentum input scheme for unresolved SNe, which is based on Blondin et al. (1998). For each explosion, we first calculate the radius of the bubble at the end of the Sedov-Taylor phase (Blondin et al. 1998)

$$R_{\rm ST} = 19.1 \left(\frac{E_{\rm SN}}{10^{51} \ {\rm erg}}\right)^{\frac{5}{17}} \left(\frac{\overline{n}}{\rm cm^{-3}}\right)^{-\frac{7}{17}} \ {\rm pc}, \quad (6)$$

where $\overline{n}$ is the mean number density within the injection region. If $R_{\rm ST} < 4\Delta x$, then we inject momentum rather than thermal energy (see also Hopkins et al. 2014). The momentum is computed from (Blondin et al. 1998)

$$p_{\rm ST} = 2.6\times10^5 \left(\frac{E_{\rm SN}}{10^{51} \ {\rm erg}}\right)^{\frac{16}{17}} \left(\frac{\overline{n}}{\rm cm^{-3}}\right)^{-\frac{2}{17}} \ {\rm M_\odot \ km \ s^{-1}}. \quad (7)$$

We deposit this momentum to the flattened density distribution within the injection region by adding the corresponding velocity of

$$v_{\rm inj} = \frac{p_{\rm ST}}{M_{\rm inj}} \ , \quad (8)$$

where $v_{\rm inj}$ points radially outwards. In addition, we increase the temperature of the injection region to 10^4 K. This guarantees that, despite the significant energy losses, the momentum input is accounted for.

This method has two caveats. i) The momentum of a SN bubble can still increase during the pressure-driven snowplough phase (Cioffi et al. 1988), which is not included in this model. ii) Due to the injection of transonic or subsonic motions, high Mach number shocks are not created and little to no hot gas is produced. Therefore, the momentum input given in equation (7) is a lower limit.

Recent results by Kim & Ostriker (2014, see also Martizzi et al. 2014; Simpson et al. 2014) indicate that the final momentum driven by a single SN explosion can be captured (within 25% of the expected value from high resolution, sub-pc simulations) under the conditions: (i) $R_{\rm ST} > 3$ $R_{\rm inj}$ and (ii) $R_{\rm ST} > 3$ Δx. This is roughly insensitive to the ambient medium density distribution. As a result, the impact of SNe exploding in density peaks might be underestimated even when $T_{\rm i,SN} > 10^6$ K for thermal energy injection. In section 3.8 we compare these requirements with our results at different resolutions.

2.5.3 Supernova positions and simulations

We will show that the positioning of the SNe relative to the gas density distribution changes the structure of the ISM. Therefore, we choose three different schemes to place the SNe: (i) random driving (runs R-$\rm n_i$), (ii) peak driving (runs P-$\rm n_i$), i.e. the current SN is placed on the global density maximum at the time, and (iii) a mixture of the two, i.e. mixed driving (runs Mf-$\rm n_i$), with a fixed ratio $f_{\rm peak}$ of peak to total SNe.

We carry out a number of simulations with different driving schemes and densities, which we summarise in Table 2. By default, we choose random driving. For this driving scheme, we run five simulations with $\dot{N}_{\rm SN,KS}$ for $n_{\rm i} = 0.5, 1, 3, 10, 30 \, \rm cm^{-3}$ and eight for $n_{\rm i} = 1, 3, 10, 30 \, \rm cm^{-3}$ with half ($\dot{N}_{\rm SN,-}$) and twice the KS SN rate ($\dot{N}_{\rm SN,+}$). In addition, we perform four simulations ($n_{\rm i} = 0.5, 1, 3, 10 \, \rm cm^{-3}$) with peak driving. For $n_{\rm i} = 3 \, \rm cm^{-3}$, we carry out 9 simulations using mixed driving with different values of $f_{\rm peak}$.

We investigate the applicability of the combined model of thermal energy and momentum injection using two simulations with $n_{\rm i} = 3 \, \rm cm^{-3}$ and $f_{\rm peak} = 100\%$ (P-C-$\rm n_3$) and 50% (M50-C-$\rm n_3$). Finally, we run two simulations for $n_{\rm i} = 3 \, \rm cm^{-3}$ at a higher resolution (with $\Delta x = 1$ pc). These runs are called R-HR-$\rm n_3$ for random and P-HR-$\rm n_3$ for peak driving.

name	$n_{\rm i}$ ($\rm cm^{-3}$)	$\dot{N}_{\rm SN}$ ($\rm Myr^{-1}$)	Driving	Note
R-n$_{0.5}$	0.5	1.2	R	
R-n$_1$	1	3	R	
R-n$_{1-}$	1	1.5	R	
R-n$_{1+}$	1	6	R	
R-n$_3$	3	14	R	
R-n$_{3-}$	3	7	R	
R-n$_{3+}$	3	28	R	
R-n$_{10}$	10	77	R	
R-n$_{10-}$	10	38.5	R	
R-n$_{10+}$	10	154	R	
R-n$_{30}$	30	360	R	
R-n$_{30-}$	30	180	R	
R-n$_{30+}$	30	720	R	
P-n$_{0.5}$	0.5	1.2	P	
P-n$_1$	1	3	P	
P-n$_3$	3	14	P	
P-n$_{10}$	10	77	P	
M10-n$_3$	3	14	M	$f_{\rm peak} = 10$
M20-n$_3$	3	14	M	$f_{\rm peak} = 20$
M30-n$_3$	3	14	M	$f_{\rm peak} = 30$
M40-n$_3$	3	14	M	$f_{\rm peak} = 40$
M50-n$_3$	3	14	M	$f_{\rm peak} = 50$
M60-n$_3$	3	14	M	$f_{\rm peak} = 60$
M70-n$_3$	3	14	M	$f_{\rm peak} = 70$
M80-n$_3$	3	14	M	$f_{\rm peak} = 80$
M90-n$_3$	3	14	M	$f_{\rm peak} = 90$
P-C-n$_3$	3	14	P	CM
M50-C-n$_3$	3	14	M	CM $f_{\rm peak} = 50$
R-HR-n$_3$	3	14	R	$\Delta x = 1$ pc
P-HR-n$_3$	3	14	P	$\Delta x = 1$ pc

Table 2. List of all simulations. From left to right: name of the simulation; initial number density of the box $n_{\rm i}$; supernova rate $\dot{N}_{\rm SN}$; Driving mode: pure random (R), pure peak (P) or mixed (M); Note: combined model with thermal energy and momentum input (CM).

2.6 Simulation analysis

The simulations are stopped once an approximate chemo-dynamical equilibrium is reached, i.e. the mass distribution of the different chemical species stays roughly constant. This is typically the case after 100–200 Myr (note that 25 Myr was the initial crossing time), depending on the initial box density and SN rate. We discuss the properties of the resulting ISM for different initial densities, driving schemes, and resolution towards the end of the simulations. In particular, we focus on four quantities:

(i) the distribution of gas mass among ionised, neutral, and molecular hydrogen;
(ii) the gas pressure in different temperature regimes;
(iii) the VFFs of gas within the different temperature regimes; and
(iv) the observable velocity dispersion.

We compute every quantity by averaging over the final 5 Myr of each simulation in order to reduce statistical errors. In Appendix A we show the full time history for three simulations with $n_{\rm i} = 3\,\rm cm^{-3}$ using random and peak driving.

To compare with velocity dispersions observed in HI and $\rm H_\alpha$, we compute the mass-weighted, one-dimensional velocity dispersion, $\sigma_{\rm avg\ 1D}$. We first compute the 1D dispersion for HI and $\rm H_\alpha$ along the x-, y-, and z-directions for each simulation:

$$\sigma_{j,k,\rm turb} = \left(\frac{\sum_i (v_{i,k} - \overline{v}_k)^2 \ m_{i,j}}{M_{j,\rm tot}} \right)^{1/2} , \qquad (9)$$

where j indicates the chemical species (HI or $\rm H_\alpha$), i is the cell index, v_i is the velocity of the cell, and $\overline{v}$ is the average velocity in the respective direction k. m_j is the mass of species j in cell i, and $M_{j,\rm tot}$ is the total mass of species j. We then average over all three directions and receive a mean, one-dimensional velocity dispersion:

$$\sigma_{j,\rm turb} = \frac{1}{3} \sum_{k=1}^{3} \sigma_{j,k,\rm turb}. \qquad (10)$$

HI VELOCITY DISPERSION: For HI the intensity is proportional to the number of emitters (e.g. Rohlfs & Wilson 1996). Therefore the HI mass is a good proxy for the total radiation flux, i.e. $M_j \propto L_j$, and the resulting velocity dispersion, $\sigma_{\rm HI,turb}$, can be considered as an intensity-weighted velocity dispersion.

$\rm H_\alpha$ VELOCITY DISPERSION: For $\rm H_\alpha$, the mass of ionised hydrogen is not a good estimate of the $\rm H_\alpha$ intensity, since the emission decreases with increasing temperature. Here, we compute the $\rm H_\alpha$ flux from two contributions, namely the recombination of ionised hydrogen and collisional excitation from the ground state to level $n = 3$. We have to neglect the contribution from HII regions around young massive stars since these are not treated in the simulations. Collisional excitations to $n > 3$ represent a negligible contribution to the total $\rm H_\alpha$ emission since transitions to these levels are significantly less likely (Anderson et al. 2000, 2002, but see also Péquignot & Tsamis (2005) and references therein). We compute $m_{\rm H\alpha}$ ($dL_{\rm H\alpha}$) and $M_{\rm tot,H\alpha}$ ($L_{\rm tot,H\alpha}$), required in eq. (9), following the emissivity calculations for recombination and collisional excitation of Draine (2011); Dong & Draine (2011), and Kim et al. (2013) (but see also Aggarwal 1983):

$$dL_{\rm H\alpha,R} \propto T_4^{-0.942-0.031\ln(T_4)} n_{\rm e} n_{\rm HII} dV , \qquad (11)$$

$$dL_{\rm H\alpha,C} \propto \frac{\Gamma_{13}(T_{\rm e})}{\sqrt{T_{\rm e}}} e^{\frac{-12.1\rm eV}{k_{\rm B} T_{\rm e}}} n_{\rm e} n_{\rm HI} dV , \qquad (12)$$

where $T_4 = T/10^4$ K, $T_{\rm e}$ is the electron temperature, n_j is the number density of species j in $\rm cm^{-3}$, dV is the zone volume, and

$$\Gamma_{13}(T_{\rm e}) = 0.35 - 2.62\times10^{-7} T_{\rm e} - 8.15\times10^{-11} T_{\rm e}^2 + 6.19\times10^{-15} T_{\rm e}^3. \qquad (13)$$

We apply equation (12) only for cells with temperatures $4000 < T < 25\,000$ K assuming $T_{\rm e} = T$. We only consider this temperature range because emission at $T < 4000$ K will be negligible, while we expect to find very little atomic hydrogen at $T > 25\,000$ K. We also assume $n_{\rm e} = n_{\rm HII}$, which results in a $\sim 10\%$ error at most in regions where helium is ionised.

We approximate the gas to be optically thin to the $\rm H_\alpha$ and HI emission. Although this assumption might lead to a poor estimate of the line intensities, we do not expect major absorption features except in cold and dense HI clouds. In this case HI self-absorption could also play a non-negligible

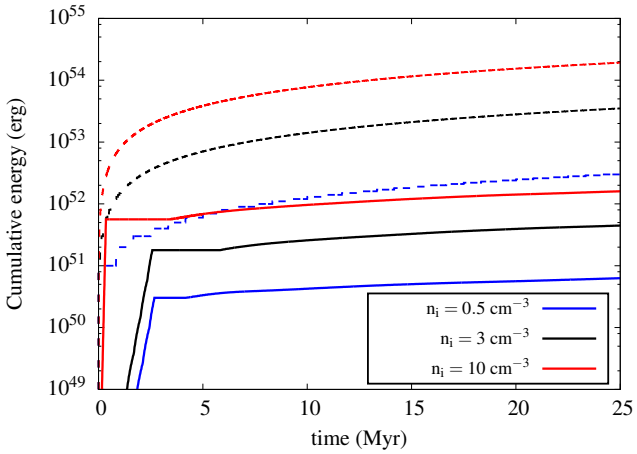

Figure 1. Cumulative energy injected in the first 25 Myr of artificial (solid lines, $t = 0 - 25$ Myr) and SN driving (dashed lines, $t = 25 - 50$ Myr) for different n_i.

role. However, as we will see in the next sections, most of the dense clumps in our models are composed of H_2, with only a small mass fraction of atomic gas in the outer shells.

THERMAL COMPONENT: We include thermal broadening by adding a mass-weighted thermal velocity

$$\sigma_{j,\mathrm{therm}} = \left(\frac{\sum_i v_{i,\mathrm{therm}}^2 \; m_{i,j}}{M_{j,\mathrm{tot}}} \right)^{1/2} , \qquad (14)$$

where $v_{i,\mathrm{therm}} = (2k_B T_i/\mu_i)^{1/2}$ with T_i being the temperature and μ_i the mean mass per particle in cell i. We assume that all species within a cell have the same temperature, which can cause small errors in the thermal velocity estimate. The resulting total velocity dispersion is

$$\sigma_{\mathrm{avg\ 1D},j} = \left(\sigma_{j,\mathrm{turb}}^2 + \sigma_{j,\mathrm{therm}}^2\right)^{1/2} . \qquad (15)$$

3 RESULTS AND DISCUSSION

3.1 Energy input

In Figure 1 we show the cumulative energy input as a function of time for artificial turbulent driving (solid lines) and SN driving (dashed lines) with a SN rate derived from the KS relation, for initial densities $n_i = 0.5, 3$ and $10\,\mathrm{cm}^{-3}$. We point out that the energy input from artificial driving necessary to maintain a constant 3D, mass-weighted, rms velocity of $v_{\mathrm{3D,rms}} = 10\,\mathrm{km\,s}^{-1}$ (corresponding to a one-dimensional velocity dispersion of $\sim 5 - 6\,\mathrm{km\,s}^{-1}$) is always about two orders of magnitude lower than the energy input in the corresponding SN-driven box. Nevertheless, we will see that SN driving is inefficient in terms of turbulence driving. Therefore, even though the energy input is high, the resulting, average, one-dimensional velocity dispersions in cold HI gas stay below $10\,\mathrm{km\,s}^{-1}$.

3.2 Impact of supernova positioning

We start from the artificially stirred, turbulent box at different densities at $t_{\mathrm{drive}} = 25$ Myr. We then evolve the simulations with SN driving at different rates and positioning of the SNe relative to the dense gas.

DENSITY AND TEMPERATURE DISTRIBUTION: In Figure 2, we compare the density and temperature structure of the ISM for three runs with $n_i = 3\,\mathrm{cm}^{-3}$ and $\dot{N}_{\mathrm{SN,KS}}$ at $t = 100$ Myr, using peak driving (run P-n$_3$, left column), random driving (run R-n$_3$, middle column), and mixed driving (run M50-n$_3$, i.e. mixed driving with $f_{\mathrm{peak}} = 50\%$, right column). The SN rate is the same and the huge differences in the ISM structure are solely due to the positioning of the SNe. For peak driving, the box is filled with warm and cold gas, which is distributed in filaments and extended clouds. There is little to no hot gas present. In the case of random driving, on the other hand, most of the box is filled with hot gas, while the cold gas is concentrated in small and dense clumps. The mixed driving case with an equal contribution from random and peak driving lies in between the other two cases. Gas at $T \gtrsim 10^6$ K occupies the majority of the box volume, but the cold and warm phases are located not just in massive clumps, but also in extended filamentary complexes.

DENSITY PROBABILITY DISTRIBUTION FUNCTIONS: In Figure 3, we show the volume-weighted probability distribution functions (PDFs) of density for the initial condition derived from artificial turbulence stirring at $t_{\mathrm{drive}} = 25$ Myr (black line) and for the three different driving modes at $t = 100$ Myr. For artificial driving at a rms velocity of 10 $\mathrm{km\,s}^{-1}$, we find a broad PDF which can be interpreted as two overlapping log-normal distributions. The medium does not consist of two distinct warm and cold phases. A significant fraction of the gas lies far from the equilibrium curve due to turbulent motions (e.g. Walch et al. 2011, but see also Vázquez-Semadeni et al. 2000; Micic et al. 2013; Saury et al. 2014). For peak driving (blue line) the PDF roughly coincides with the one for artificial driving at high densities, but with a more extended tail towards low densities. In the case of random driving (red line), the distribution has a strong peak at low densities ($\rho \sim$ few $\times\, 10^{-26}$ g cm^{-3}), which corresponds to the hot, over-pressured phase, followed by two subsequent peaks at higher densities. The maximum density reached is well above the ones produced by other driving modes. Since most of the volume is filled with hot gas, the volume-weighted PDF is dominated by a single peak at low densities. Mixed driving (green line) displays an intermediate distribution between random and peak driving with three broad peaks. This is typical for a turbulent three-phase ISM consisting of cold, warm and hot gas, with significant contributions from each component (e.g. Gent et al. 2013).

PHASE DIAGRAMS: In Figure 4, we show exemplary $\rho - T$ and $\rho - P$ phase diagrams for random and peak driving, where the mass distribution is colour-coded. In the random driving case (top row) the gas is moved to high pressures $P/k_B \gtrsim 10^4$ K cm^{-3}, which is above the mean pressure in the Milky Way (e.g. Jenkins & Tripp 2011). A small fraction of the gas reaches high temperatures $T > 10^6$ K; this gas occupies virtually all of the volume, as shown in Figure 3. This hot, high-pressure gas pushes the majority of the mass into the cold, dense phase (see section 3.3). The cold, high density tail lies slightly below the equilibrium curve. A likely explanation is that at high density, the cold gas is efficiently shielded against the far-UV interstellar radiation field. Since the equilibrium values are computed without considering this mechanism, the densest component has a lower equilibrium pressure and temperature in this density range.

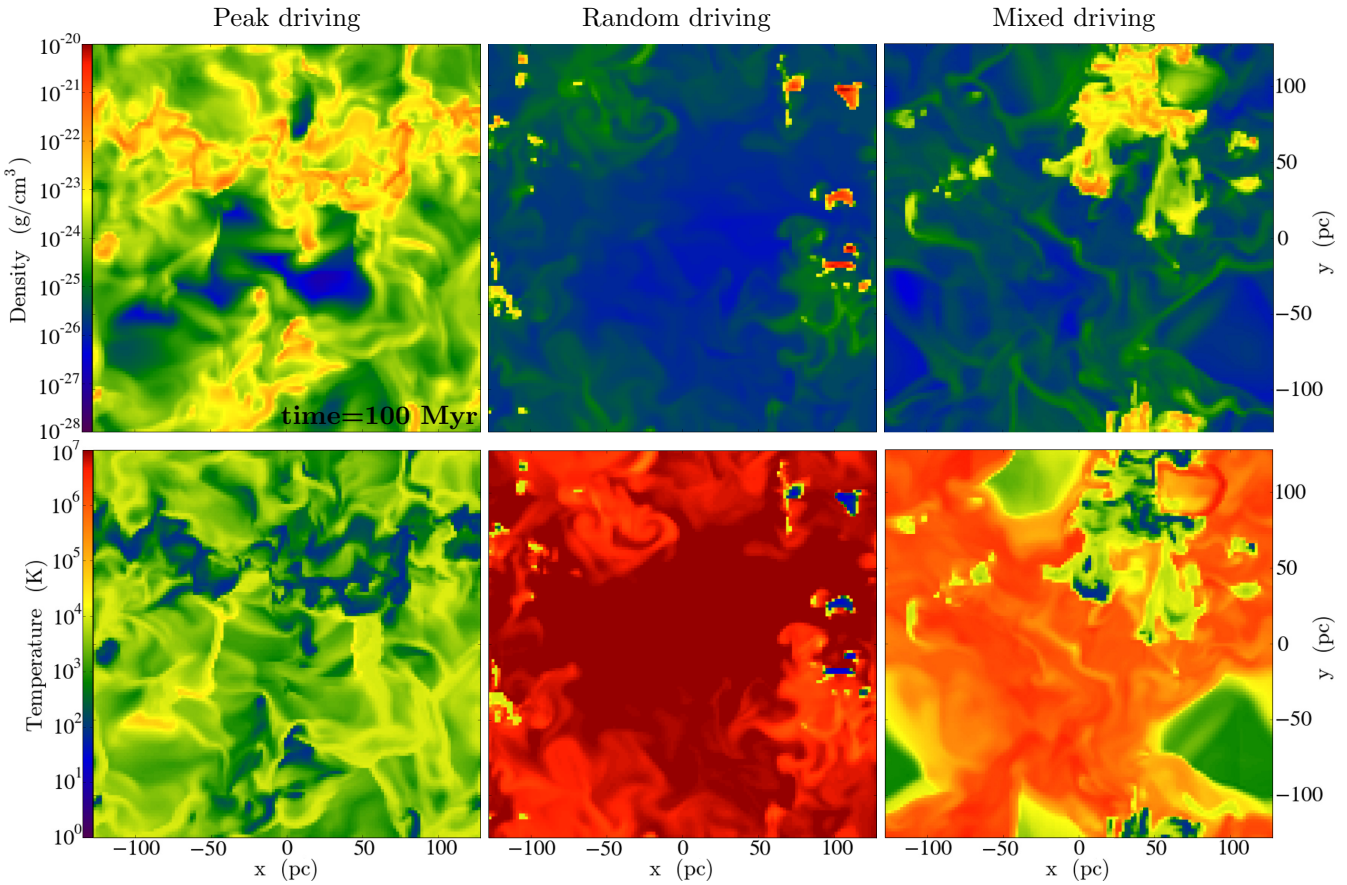

Figure 2. Density (top row) and temperature (bottom row) slices for three runs with initial density $n_\mathrm{i} = 3\,\mathrm{cm}^{-3}$ and SN rate drawn from the Kennicutt-Schmidt relation $\dot{N}_\mathrm{SN,KS}$. From left to right, we show runs P-n$_3$ (peak driving), R-n$_3$ (random driving) and M50-n$_3$ (mixed driving with $f_\mathrm{peak} = 50\%$) at $t = 100$ Myr.

On the other hand in the peak driving case (bottom row) a two-phase medium, with warm and cold gas in approximate pressure equilibrium, is formed. The densest component actually lies slightly above the equilibrium curve due to the continuous heating of the densest gas parcels by SN shocks. However, these simulations contain little to no hot gas, as the SNe, which explode only in dense environments, fail to effectively heat the gas (see section 3.5). The maximum densities reached in simulations with peak driving are 1–2 orders of magnitude smaller than in the random driving case since, by construction, peak driving removes the densest component of the medium and highly over-pressured hot regions are not present in this case.

Summary: We may summarise the impact of the different SN positioning (see Figs. 2 and 4) as follows: in the case of random driving, most SNe are placed in positions where their energy can be efficiently transferred to the ISM. In the case of peak driving, the SNe explode in dense gas, which may promptly radiate a large fraction of the inserted energy. The higher the fraction of random SNe, the more efficiently energy is injected, which increases the thermal gas pressure and increases the chance to end up in a thermal runaway regime, as discussed in the next subsection. In section 3.6 we explore this transition in simulations with different f_peak.

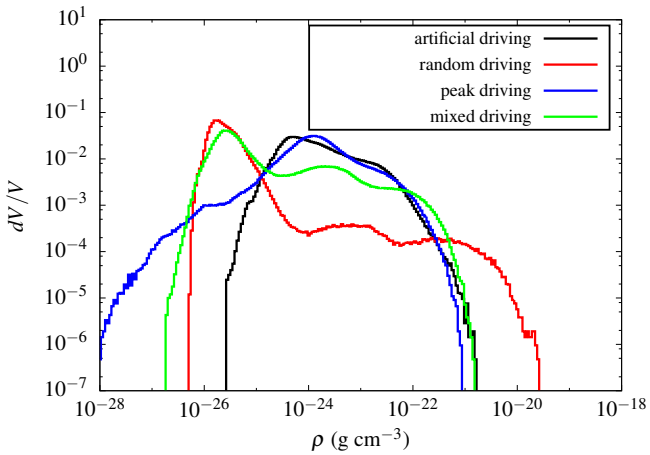

Figure 3. Volume-weighted density PDFs for different driving modes, i.e. random (red line), peak (blue line), and 50% mixed driving (green line), for the n$_i$ = 3 cm^{-3} runs at $t = 100$ Myr. In addition, we show the initial condition from artificial stirring at $t_\mathrm{drive} = 25$ Myr (black line).

3.3 Thermal runaway

The high pressure reached in our models results in the equilibrium between heating and cooling lying not in the regime

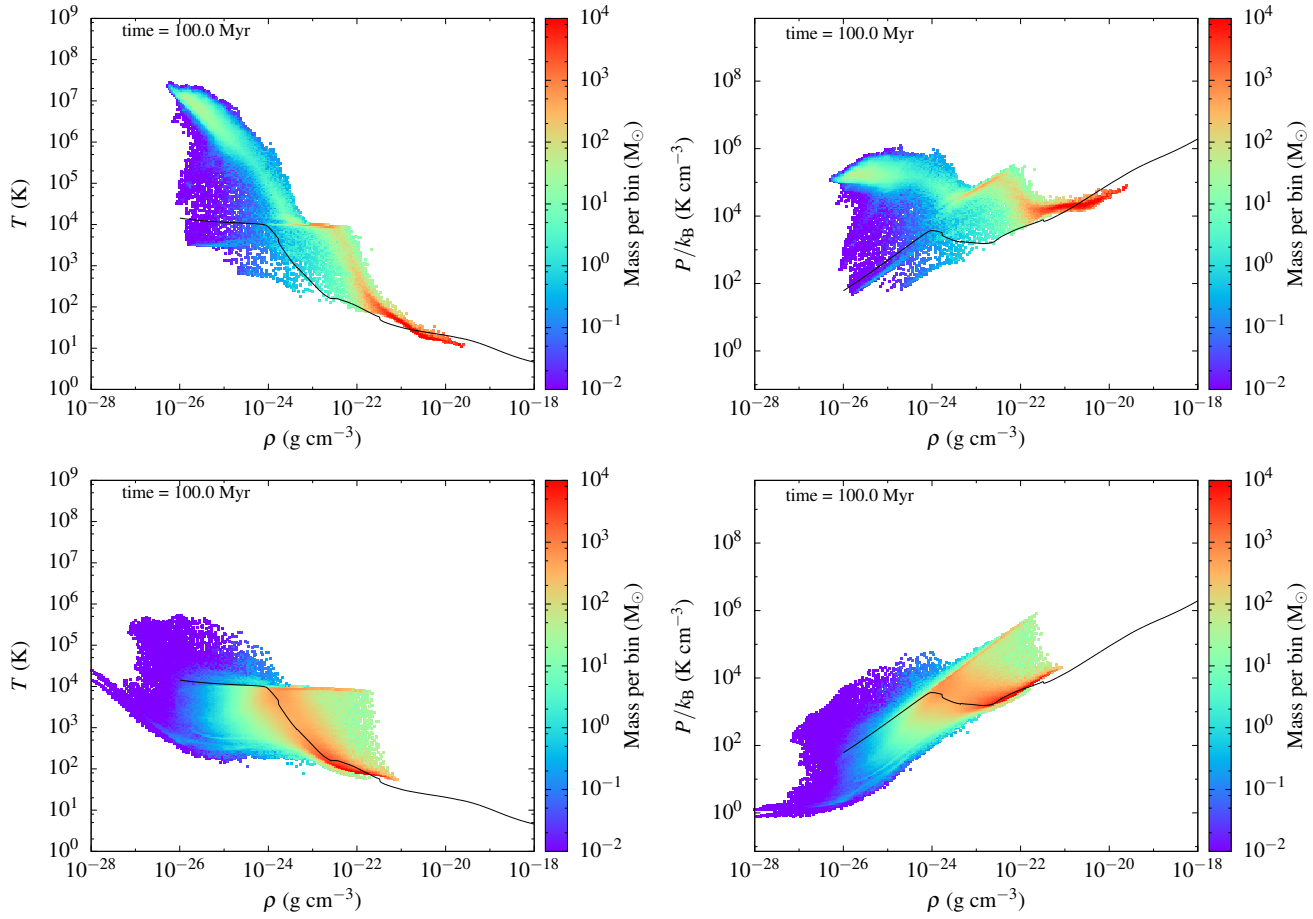

Figure 4. Density-temperature (left) and density-pressure (right) phase diagrams for two simulations with initial density $n_{\rm i} = 3\,{\rm cm}^{-3}$ and $\dot{N}_{\rm SN,KS}$ at $t = 100$ Myr. We colour-code the mass distribution. The first row shows run R-n$_3$ (random driving), while the second row shows run P-n$_3$ (peak driving). The solid lines show where radiative cooling and diffuse radiative heating reach equilibrium.

near $P/k_B \sim 10^3$ K cm^{-3} where a two-phase medium is possible, but rather on the cold branch of the equilibrium curve, where balance between heating and cooling can only be reached at low temperatures and high densities. This explains why virtually all the mass lies at high density ($n > 100$ cm^{-3}) and low temperature ($T < 200$ K). As a result, we move from the classic paradigm of a two-phase medium in pressure equilibrium towards a scenario in which only the cold phase survives, consistent with the picture of Wolfire et al. (1995) for high heating (far-UV interstellar field) rates. The cooling times in the remaining rarefied gas are long, since radiative cooling is proportional to n^2 and drops significantly for temperatures above 10^6 K (Raymond et al. 1976). As a result, almost all of the volume is occupied by gas with low density and $T > 10^6$ K, whose cooling time far exceeds the dynamical time of the system: the third phase of the three-phase medium (McKee & Ostriker 1977). This picture is consistent with the findings of Scannapieco et al. (2012), who use hydrodynamical simulations of artificially-driven turbulence in a stratified disc to mimic the impact of stellar feedback. They find that, for turbulent one-dimensional velocity dispersions $\gtrsim 35\,{\rm km\,s}^{-1}$, large fractions of gas are continuously heated and unable to cool within a turbulent crossing time. This process leads to powerful outflows and compression of cold gas. In the thermal runaway regime, our simulations behave in a similar way, as energy is directly deposited into a hot, high pressure medium, with a resulting one dimensional velocity dispersion of the hot phase well above the critical value of $35\,{\rm km\,s}^{-1}$.

The high pressures reached in the thermal runaway regime marks a clear distinction from the classic picture of McKee & Ostriker (1977). In that model, a SN remnant expands into a medium characterised by the presence of many evenly-distributed, small, two-phase clouds having cold cores surrounded by warm envelopes. The passage of the SN blast wave heats and destroys these clouds, sweeping them up into a dense shell. This dense shell cools and slows down during the radiative phase, and the remnant ceases to exist when it reaches pressure equilibrium with the ambient medium. For thermal runaway, however, SNe go off in a hot, high pressure environment, while isolated cold clouds lie far from the explosion position. Well before the end of the Sedov-Taylor phase, the remnants reach pressure equilibrium with the hot gas and deposit their energy into the medium without any significant radiative loss.

In this environment heating cannot be balanced by radiative cooling. In our periodic box, within which there is no vertical stratification to allow an atmosphere to evolve into hydrostatic equilibrium with a galactic potential, the hot gas pressure can only be set by the balance between cooling and

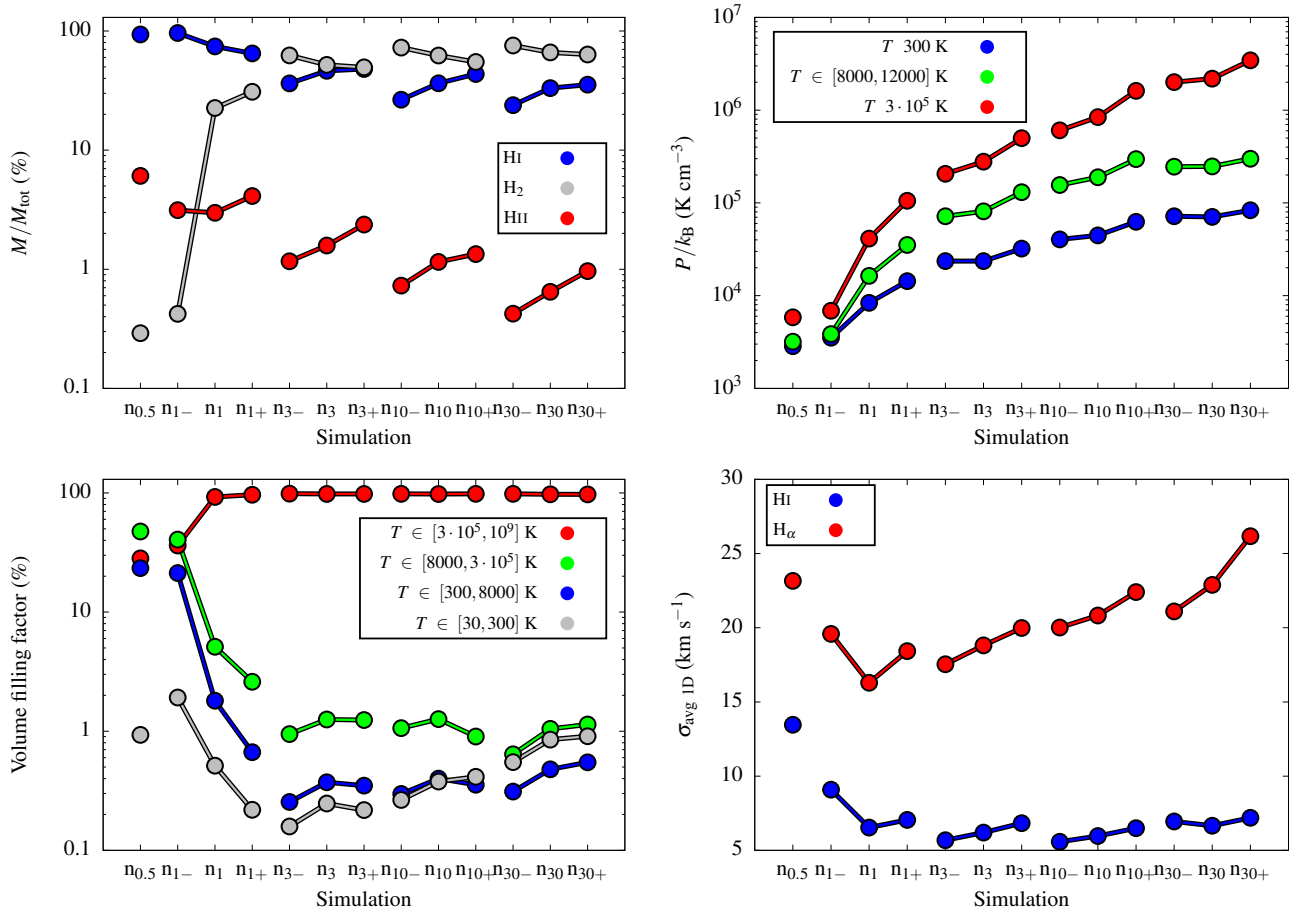
$M/M_{\rm tot}$ (%)
HI
H_2
HII
$P/k_{\rm B}$ (K cm^{-3})
T 300 K
$T \in [8000, 12000]$ K
T $3 \cdot 10^5$ K
Volume filling factor (%)
$T \in [3 \cdot 10^5, 10^9]$ K
$T \in [8000, 3 \cdot 10^5]$ K
$T \in [300, 8000]$ K
$T \in [30, 300]$ K
$\sigma_{\rm avg\ 1D}$ (km s^{-1})
HI
H_α
$n_{0.5}$ n_{1-} n_1 n_{1+} n_{3-} n_3 n_{3+} n_{10-} n_{10} n_{10+} n_{30-} n_{30} n_{30+}
Simulation

Figure 6. Average mass fractions (top left), pressures (top right), VFFs (bottom left) and 1D velocity dispersions (bottom right) with random driving for different initial densities $n_{\rm i}$ and SN rates. The index i represents the initial number density, while the + and − signs give the SN rate ($\dot{N}_{\rm SN,+}$ and $\dot{N}_{\rm SN,-}$). The values are averaged over the last 5 Myr (section 2.6). The different lines connect simulations with same $n_{\rm i}$ but different SN rate.

heating. Random driving thus pushes the system towards a thermal runaway regime, where the hot gas contains most of the energy, while the majority of the box mass is stored in the coldest phase without the possibility to return to a system with a significant warm phase ($T \sim 10^4$ K). Cold gas is not formed from a two-phase medium, but instead cools directly to the cold branch of the equilibrium curve, forming high-density clumps with small VFF. The cold clumps are produced by compression waves coming from the hot, high-pressure gas. This mechanism causes an efficient and fast conversion from warm, atomic gas to molecular. These clumps are resolved by so few zones that they cannot reach high enough densities to remain in pressure equilibrium with the background. As a result, cold clouds at low pressures are embedded into a hot, high-pressure environment. This numerically caused jump in pressure can reach about one order of magnitude (see Fig. 5 for the pressure distribution in run with $n_{\rm i} = 3\,{\rm cm}^{-3}$ and $\dot{N}_{\rm SN,KS}$). Therefore, we must treat the interior properties of the clouds as limits at low density and velocity dispersion, rather than converged values.

3.4 Random driving at different SN rates

In this section we discuss the properties of the ISM forming in runs R-n$_{\rm i}$ with randomly placed SNe and different initial densities $n_{\rm i}$. The SN rates are adjusted to the given $n_{\rm i}$ (see section 2.4). We perform three simulations with different SN rates for almost every $n_{\rm i}$ using $\dot{N}_{\rm SN,KS}$, and $\dot{N}_{\rm SN,-}$ and $\dot{N}_{\rm SN,+}$, where the SN rate is decreased/increased by a factor of two, respectively (see also Table 1). In Figure 6 we compare the different simulations. We plot the mass in ionised, atomic, and molecular hydrogen (top left panel), the pressure in three different temperature regimes, which are representative for the cold, warm ionised, and hot phase of the ISM (top right), the VFF in different temperature phases (bottom left), and the velocity dispersion of the gas in HI and H_α (bottom right) towards the end of each simulation. To guide the eye we connect the simulations with equal $n_{\rm i}$ but different SN rate.

CHEMICAL COMPOSITION: We follow the chemical evolution of the gas, including the formation of molecular hydrogen, taking into account the effects of dust shielding and molecular (self-)shielding. We find that the mass in ionised hydrogen is always below 10% and decreasing for increas-

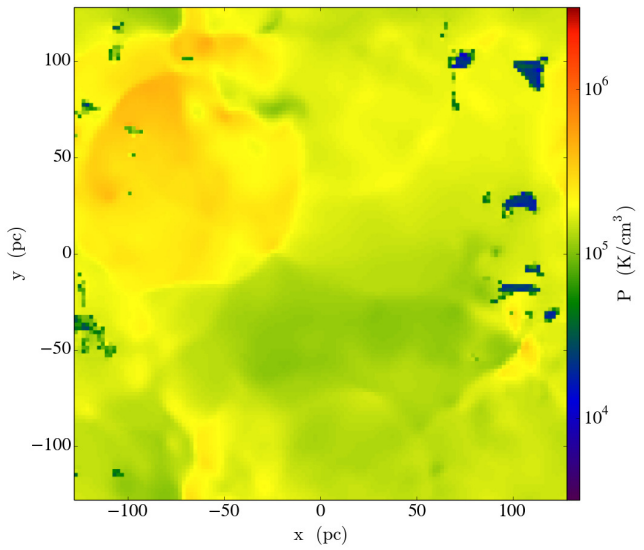

Figure 5. Pressure slice for the random driving run with initial density $n_\mathrm{i} = 3\,\mathrm{cm}^{-3}$ and $\dot{N}_\mathrm{SN,KS}$ at $t = 100$ Myr (see also central column of Fig. 2).

ing box density. For low densities ($n_\mathrm{i} \lesssim 3\,\mathrm{cm}^{-3}$) most of the total mass is in atomic hydrogen. At higher densities ($n_\mathrm{i} \gtrsim 3\,\mathrm{cm}^{-3}$) less than 50% of the mass is in HI and the rest is in molecular hydrogen. Molecular hydrogen, which is organised in small, dense clumps (see Fig. 2), dominates the mass budget at high densities and SN rates (up to 80% of the total mass is in form of H_2 at $n_\mathrm{i} = 30\,\mathrm{cm}^{-3}$).

GAS PRESSURE: We compute the average pressure in three different temperature regimes: (i) for the stable cold phase at $T \leqslant 300$ K; (ii) for the stable warm phase at $8000 \leqslant T \leqslant 12000$ K; and (iii) for the hot phase at $T \geqslant 3{\cdot}10^5$ K. For $n_\mathrm{i} \leqslant 1\,\mathrm{cm}^{-3}$ the medium is roughly in pressure equilibrium, but for higher densities and SN rates the pressures of the three phases diverge slowly as we get into the thermal runaway regime.

VOLUME FILLING FRACTIONS: We show the VFFs of the gas in the bottom left panel of Figure 6. We distinguish four different temperature regimes: the cold phase at $30 \leqslant T < 300$ K; the warm atomic ISM at $300 \leqslant T < 8000$ K; the warm ionised medium at $8000 \leqslant T < 3 \times 10^5$ K; and the hot ionised medium at $T \geqslant 3 \times 10^5$ K. Only for two simulations (R-n$_{0.5}$ and R-n$_{1-}$), are the VFFs close to what we expect for a Milky Way-type galaxy near the mid-plane (e.g. Kalberla & Dedes 2008; Kalberla & Kerp 2009), whereas the hot gas fills most of the volume at higher densities and/or SN rates.

We compare the VFFs of the hot ionised medium with the analytic prediction of McKee & Ostriker (1977). The volume occupied by SN remnants at random locations in a uniform medium, f, can be written as

$$f = 1 - e^{-Q} \ , \tag{16}$$

with porosity Q defined as

$$Q = 10^{-0.29} E_{51}^{1.28} S_{-13} \bar{n}^{-0.14} \tilde{P}_{04}^{-1.3} \ , \tag{17}$$

where E_{51} is the SN energy normalised to 10^{51} erg, S_{-13} is the SN rate in units of 10^{-13} pc^{-3} yr^{-1}, $\bar{n}$ is the number density of the ambient medium in cm^{-3}, and $\tilde{P}_{04} = 10^{-4} P_0 / k_\mathrm{B}$, with P_0 and k_B ambient medium pressure and Boltzmann constant, respectively.

We find a reasonable agreement of the VFF for models R-n$_{0.5}$ and R-n$_{1-}$, where $f \sim 30\%$ - 40%. However, the analytic model predicts lower hot gas VFFs for higher densities and SN rates such than the ones found in our higher SN rate simulations. Since $Q \propto \bar{n}^{1.26} \tilde{P}_{04}^{-1.3}$, f as derived from eq. (16) and (17) is roughly constant, whereas the simulation shows it increasing towards unity in the thermal runaway regime.

HI AND H_α VELOCITY DISPERSION: In the bottom right panel of Figure 6, we show the velocity dispersions in HI, $\sigma_{\mathrm{avg\ 1D}}(\mathrm{HI})$, and H_α, $\sigma_{\mathrm{avg\ 1D}}(H_\alpha)$. For $n_\mathrm{i} \leqslant 1\,\mathrm{cm}^{-3}$ and, in particular, for low SN rates ($\dot{N}_\mathrm{SN} \lesssim 2$ Myr^{-1}), SNe are able to inject the observed level of turbulence in the HI gas, while $\sigma_{\mathrm{avg\ 1D}}(\mathrm{HI}) \sim 5 - 7\,\mathrm{km\,s}^{-1}$ for $n_\mathrm{i} > 1\,\mathrm{cm}^{-3}$. Due to the small size of most cold clumps, these values are a mixture of the clump-to-clump velocity dispersion and thermal broadening, rather than being a measure of the disordered motions within these clouds. For the H_α dispersion, we find a similar trend going from SN rates of $\dot{N}_\mathrm{SN} \lesssim 2$ Myr^{-1} to slightly higher ones. First $\sigma_{\mathrm{avg\ 1D}}(H_\alpha)$ drops from ~ 24 km s^{-1} to ~ 17 km s^{-1}, but then it increases slowly with increasing box density and SN rate and is ~ 26 km s^{-1} for $n_\mathrm{i} = 30$ cm^{-3} and high SN rates.

3.5 Peak driving vs. random driving

We perform simulations using peak driving (runs P-n_i) at the same box densities and SN rates as in the corresponding runs with random driving (see Table 2). In Figure 7 we show the resulting ISM properties with respect to the random driving case.

CHEMICAL COMPOSITION: The peak driving runs are dominated by atomic rather than molecular gas. The H_2 mass fraction is low for two reasons: (i) the densest peaks are dispersed by SNe and, therefore, H_2 is locally dissociated; and (ii) the strong compressive SN shocks, which are widespread in the case of random driving, are localised in the immediate neighbourhood of the SN for peak driving. The destruction of molecular gas from peak SNe is broadly consistent with the findings of Hennebelle & Iffrig (2014) and Iffrig & Hennebelle (2014), where SNe exploding close to or within star formation sites can disperse cold and dense gas. In addition, the inefficient heating by peak SNe further reduces the small fraction of mass in the form of thermally ionised hydrogen.

GAS PRESSURE: We find lower pressures for peak driving, in particular for the warm and cold gas components. However, the pressure of the hot phase ($T \geqslant 3 \times 10^5$ K) appears to be significantly higher (by a factor of ~ 10) in case of peak driving at $n_\mathrm{i} \geqslant 3$ cm^{-3}. This increase has to be interpreted in conjunction with the decreasing VFF of the hot gas at these densities. Since the SNe, which explode in high density environments, are subject to strong radiative cooling, the high pressure reflects the young age of the SN remnants that do contribute to the hot phase.

VOLUME FILLING FRACTIONS: Peak driving does not produce a predominantly hot ISM. Instead, the VFF is highest for the warm and cold atomic phases. In particular for

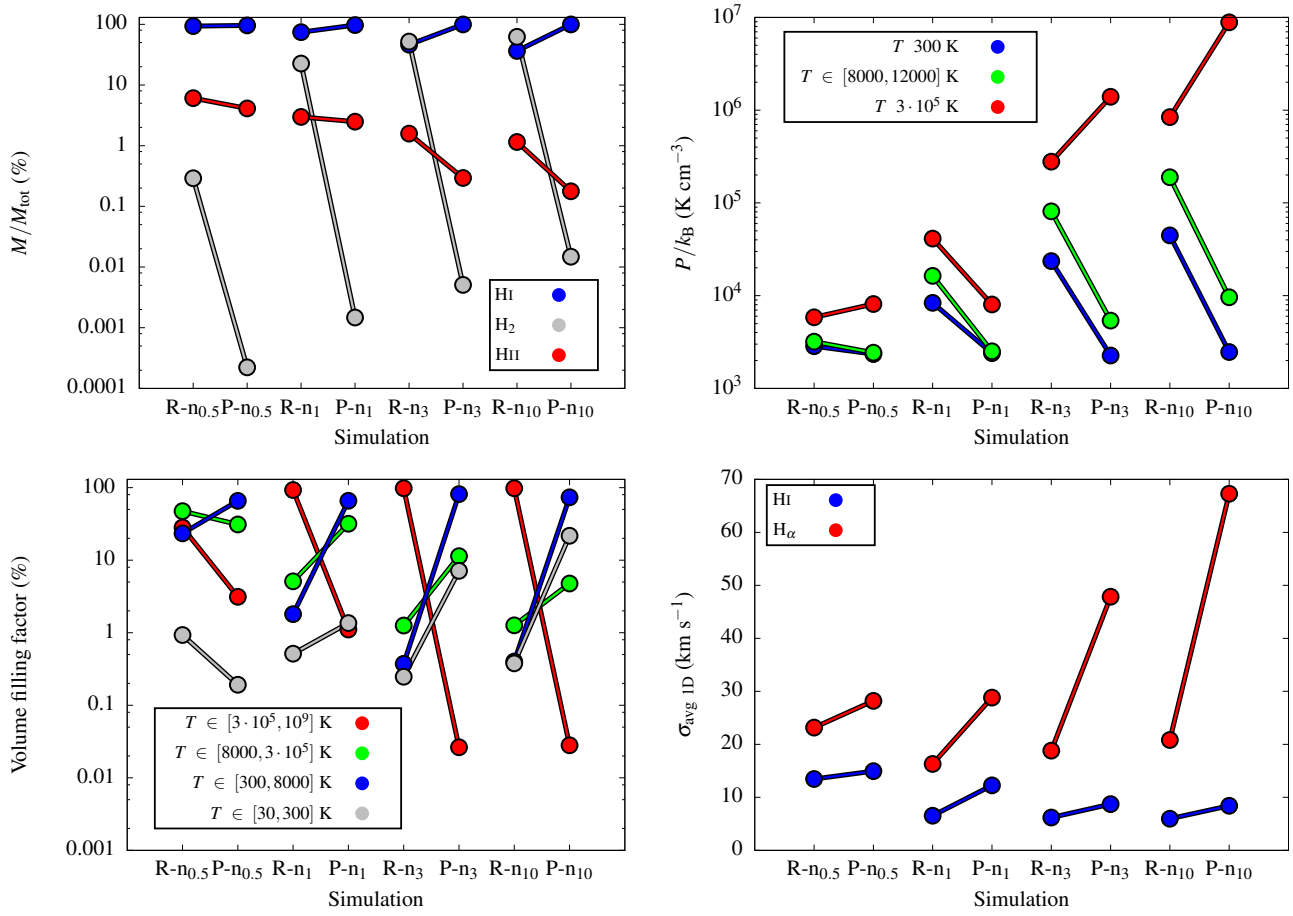

Figure 7. Average mass fractions (top left), pressures (top right), VFFs (bottom left) and 1D velocity dispersions (bottom right) with random (R) and peak (P) driving for different initial densities $n_{\rm i}$, using the corresponding $\dot{N}_{\rm SN,KS}$. The lines connect simulations with equal $n_{\rm i}$ and SN rate but different driving modes (R or P).

low densities, a non-negligible contribution is also produced by the warm ionised medium, but the VFF of this component decreases with increasing density, similar to the case of random driving. In general, the absence of a significant hot phase reflects the small sphere of influence of each peak SN, whose expansion is stopped early on due to strong radiative cooling.

HI AND H_α VELOCITY DISPERSION: In the case of peak driving, the HI velocity dispersion is slightly higher than for random driving. This is reasonable since the SNe deposit momentum into the cold gas. The velocity dispersion of the warm ionised gas as seen in H_α grows even more significantly up to $50 - 70$ km s^{-1} for $n_{\rm i} \geqslant 3$ cm^{-3}. As we have seen, the hot and warm ionised gas are found in the earliest stages of the SN remnants, which otherwise cool efficiently. Thus, the apparent high values of the H_α velocity dispersion stem from the integration over a number of isolated, compact, young SN remnants.

3.5.1 Discussion: Is peak driving realistic?

Figure 7 shows that peak driving efficiently disperses cold gas. The SNe which, by choice, explode in the densest environments, are subject to strong radiative cooling. For this reason, peak driving fails to reproduce both the VFF of hot gas and the large molecular gas mass fractions characteristic of the Milky Way (Ferrière 2001). The absence of hot gas is also inconsistent with the expectation of SNe being responsible for the creation of a hot phase (McKee & Ostriker 1977).

We can conclude that pure peak driving does not reproduce realistic ISM conditions – probably because we neglect other important physical ingredients, such as clustering and stellar feedback mechanisms, i.e. pre-SN feedback like stellar winds and ionising radiation (Walch et al. 2012). However, one has to be cautious not to over-estimate the effect of radiative cooling due to the finite numerical resolution of our models. Numerical over-cooling acting at the interface between the cold shell and the hot interior of a SN bubble may reduce the amount of hot gas. More importantly, the density and, therefore, the mass within the SN injection region is high in case of peak driving. Since we always inject a SN energy of 10^{51} erg per explosion, the effective temperature within the injection region can drop below 10^6 K in a dense environment. This is an unfavourable temperature regime, the cooling curve is steep and the heated SN gas can be cooled efficiently.

Figure 8 shows the approximate initial temperatures (from eq. 5) of all SNe in case of $n_{\rm i} = 3\,{\rm cm}^{-3}$ and $\dot{N}_{\rm SN,KS}$ for run R-n_3 with random and run P-n_3 with peak driving. The

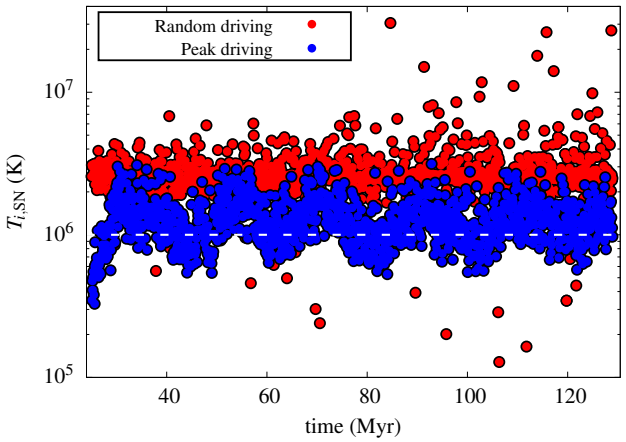

Figure 8. Initial temperature of SNe estimated from equation (5) for pure peak and random driving with $n_i = 3\,\mathrm{cm}^{-3}$ and $\dot{N}_{\mathrm{SN,KS}}$.

temperature within the injection region, $T_{\mathrm{i,SN}}$, depends on the density. Typically, the temperature is $T_{\mathrm{i,SN}} > 2 \times 10^6$ K in case of random driving. For peak driving we find $T_{\mathrm{i,SN}} \gtrsim 10^6$ K, and for ∼35% of all explosions the temperature is below 10^6 K, leading to immediate strong cooling. For this reason, we explore a combined energy and momentum input model in section 3.7.

3.6 Mixed driving

Peak and random driving represent two extreme cases of what we expect for the spatial distribution of SNe. To examine intermediate cases, we perform 9 additional simulations with $n_i = 3\,\mathrm{cm}^{-3}$ and $\dot{N}_{\mathrm{SN,KS}}$ and different values of f_{peak}, the fraction of SNe going off in dense gas. Here, $f_{\mathrm{peak}} = 0\%$ corresponds to random driving and $f_{\mathrm{peak}} = 100\%$ corresponds to peak driving. In Figure 9 we show the mass fractions (top left), pressures (top right), VFFs (bottom left) and 1D velocity dispersions (bottom right) as a function of f_{peak}.

Chemical composition: The ratio of atomic to molecular gas has a steep transition at $f_{\mathrm{peak}} \approx 50\%$. For $f_{\mathrm{peak}} > 50\%$ the box is HI-dominated, which is typical for an ISM where the coldest component is removed by SN explosions within the dense gas. On the other hand, for $f_{\mathrm{peak}} < 50\%$, we find large amounts of molecular hydrogen since (i) a smaller f_{peak} disperses fewer dense clumps, and (ii) the larger number of uncorrelated SNe heat up the gas around the dense and cold medium and compress it (see section 3.3).

Gas pressure: We find that all three phases are out of pressure equilibrium, although the pressures of the cold and warm phases decrease with increasing f_{peak} and these phases become close to isobaric for $f_{\mathrm{peak}} > 50\%$. However, the hot gas pressure diverges for $f_{\mathrm{peak}} > 50\%$ as the SN remnants which contribute to this phase become younger and occupy smaller volumes. This has already been discussed for the case of pure peak driving (see section 3.5).

Volume Filling Fractions: A sharp transition at $f_{\mathrm{peak}} \approx 50\%$ can also be found for the VFFs of the different gas phases. For $f_{\mathrm{peak}} \gtrsim 50\%$, the hot gas VFF drastically decreases while the VFFs of the warm and cold components are increasing. For small $f_{\mathrm{peak}} < 50\%$ the number of random SN explosions is high enough to fill most of the box with hot gas and drive the box towards the thermal runaway regime.

HI and H_α velocity dispersion: With increasing peak fraction, the HI velocity dispersion increases from $\sim 5-6$ km s^{-1} to $\sim 8-9$ km s^{-1} at $f_{\mathrm{peak}} \approx 40\%$. Also the H_α velocity dispersion increases for $f_{\mathrm{peak}} \gtrsim 40\%$, from ~ 18 km s^{-1} to ~ 48 km s^{-1} for $f_{\mathrm{peak}} = 100\%$. For high f_{peak}, most of the H_α-emitting gas comes from young SN remnants (see section 3.5).

3.6.1 Discussion: the transition between the peak and random driving regime.

Mixed driving, i.e. a combination of peak and random driving at different ratios, shows a relatively sharp transition in most ISM properties at a critical ratio of $f_{\mathrm{peak,crit}} \approx 50\%$. It is likely that $f_{\mathrm{peak,crit}}$ depends on the box density and SN rates. For instance, we expect $f_{\mathrm{peak,crit}}$ to shift to higher values for higher average densities. It is also likely that $f_{\mathrm{peak,crit}}$ shifts towards lower values if the periodic boundary conditions are relaxed and the box is allowed to 'breathe' (i.e. to adjust to local pressure equilibrium as gas is allowed to escape the box). In this case the thermal runaway can also be delayed, leading to small $f_{\mathrm{peak,crit}}$, or even avoided altogether. Thus, rather than being interested in extrapolating detailed physical conclusions, we are more keen on stressing once again that there are major differences in the properties of the ISM, which results from implementations of either peak or random driving.

3.7 Combined thermal energy and momentum injection

Due to our finite numerical resolution, the injection of thermal energy alone might lead to over-cooling in dense regions (see section 3.5.1 and Figure 8). Therefore, we introduce a SN model, which allows us to switch from thermal energy to momentum input when the density in the vicinity of the SN is high and the Sedov-Taylor phase is unresolved (see section 2.5.2). Using two simulations, we discuss how the combined model performs with respect to the thermal energy injection scheme. In particular, we redo run P-n$_3$, i.e. peak driving at $n_i = 3\,\mathrm{cm}^{-3}$, and run M50-n$_3$, i.e. mixed driving with $f_{\mathrm{peak}} = 50\%$ and $n_i = 3\,\mathrm{cm}^{-3}$. The corresponding new runs, which use the combined model, are called P-C-n$_3$ and M50-C-n$_3$.

The comparison between runs with and without momentum input suffers from uncertainties in the resolution of peak SNe with thermal energy injection. If unresolved, these SNe are prone to cool too quickly and the resulting momentum input could be underestimated (see section 2.5.2 and 3.8). On the other hand, the momentum injection method only takes into account the momentum-generating Sedov-Taylor phase and neglects the additional contribution from the pressure-driven snowplough phase (section 2.5.2). Due to these intrinsic differences, a very detailed comparison is not possible at the moment.

In Figure 10 (left panel) we show that the Sedov-Taylor radius (eq. 6) is unresolved, i.e. $R_{\mathrm{ST}} < 4\Delta x$ as indicated by the green dashed line, for all SNe in run P-C-n_3 and for 63% of the SNe in M50-C-n_3. In the latter case, the percentage

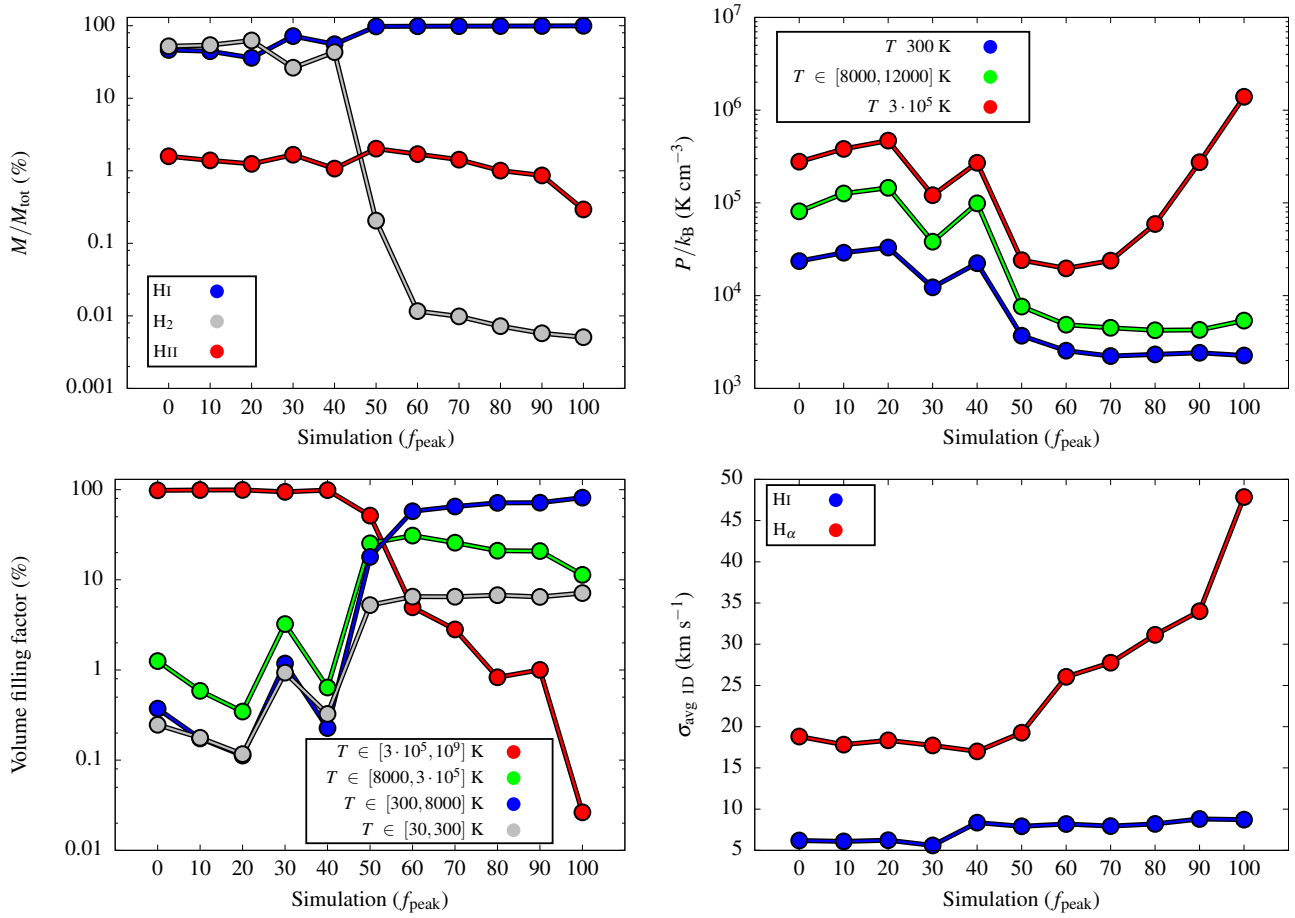

Figure 9. Average mass fractions (top left), pressures (top right), VFFs (bottom left) and 1D velocity dispersions (bottom right) as a function of $f_{\rm peak}$ for simulations using $n_{\rm i} = 3\,{\rm cm}^{-3}$ and $\dot{N}_{\rm SN,KS}$.

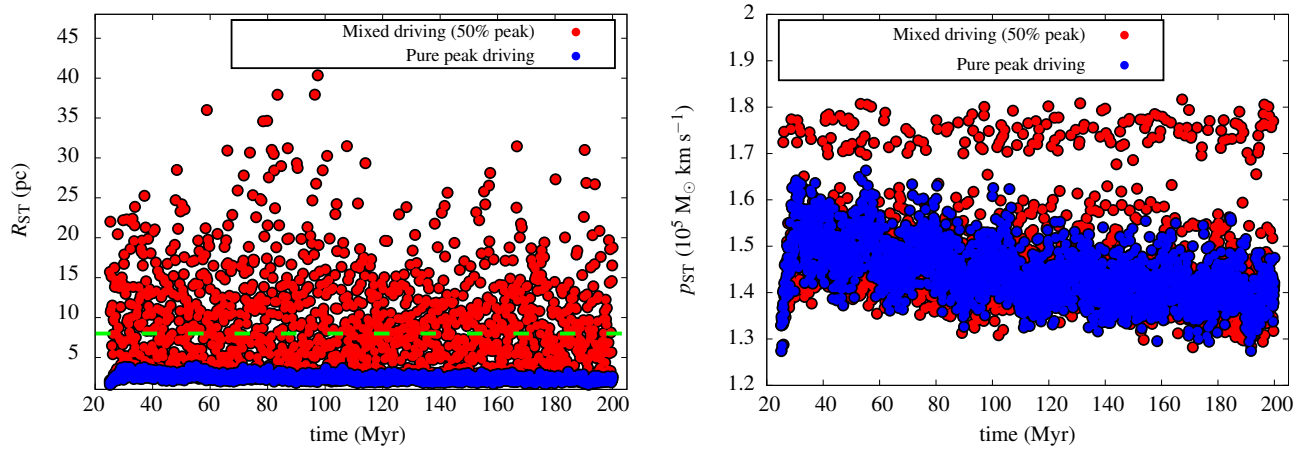

Figure 10. Radius at the end of the Sedov-Taylor phase (eq. 6; left) and injected momentum (eq. 7; right) for runs with pure peak driving (run P-C-n$_3$) and mixed driving with $f_{\rm peak} = 50\%$ (run M50-C-n$_3$). The dashed lines shows the resolution limit of $4\Delta x$, below which SNe are modelled via momentum input.

of unresolved SNe being > 50 % reflects the fact that most random SNe explode in a low density environment, but not all of them. For the unresolved SNe, the injected momentum varies between $1 - 2 \times 10^5$ M$_\odot$ km s^{-1}, as shown in the right plot of Figure 10. On a side note, if we instead require that the temperature within the injection region is higher than 10^6 K, we find that $R_{\rm ST}$ as given in eq. (6) is somewhat conservative and could safely be increased by a factor of ~ 1.6.

In Figure 11 we compare the properties of the resulting

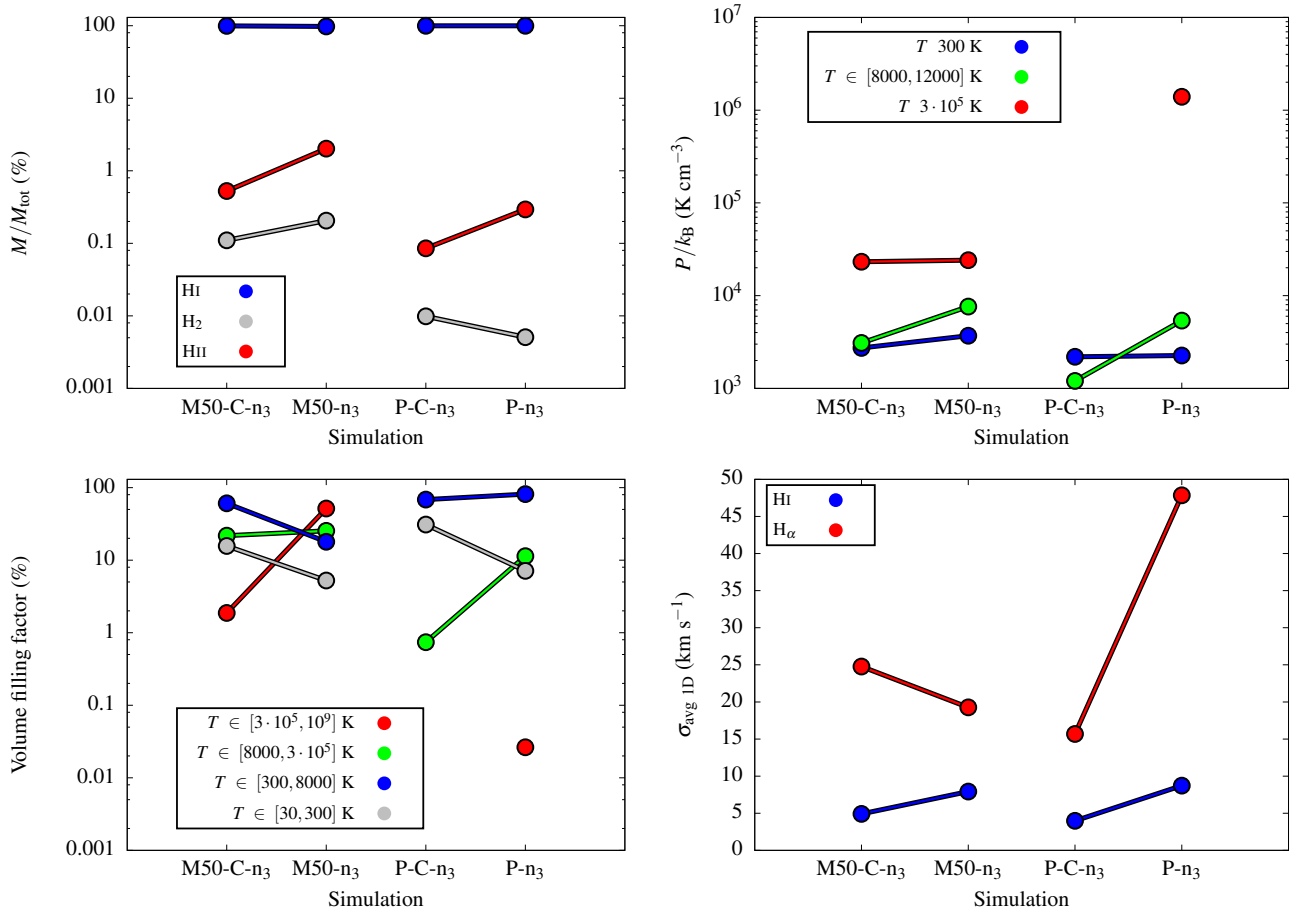

Figure 11. Average mass fractions (top left), pressures (top right),VFFs (bottom left) and 1D velocity dispersions (bottom right) for the momentum input simulations with $n_{\rm i} = 3\,{\rm cm}^{-3}$ and $\dot{N}_{\rm SN,KS}$. The points are: mixed driving with 50% peak with combined thermal and momentum injection (M50-C-n$_3$); mixed driving with 50% peak with thermal energy injection (M50-n$_3$); pure peak driving with combined injection (P-C-n$_3$); pure peak driving with thermal energy injection (P-n$_3$). The values are the average over the last 5 Myr of each simulation. The different lines connect simulations with same $n_{\rm i}$, SN rates, and driving modes, but different injection methods.

ISM for runs with pure thermal energy injection and the new combined SN scheme. Here, the lines connect the models with the old and the new combined model.

Chemical composition: For both cases (peak and mixed driving), the two SN injection schemes give comparable mass fractions in all species. There are small differences, but these are well within the statistical fluctuations in the time evolution of each component (see Appendix for a discussion on the fluctuations).

Gas pressure: The main difference between the thermal energy injection and the combined SN injection scheme is that there is no hot gas present in case of the combined model, if all the SNe are using the momentum input scheme. This is the case for run P-C-n$_3$ (see also Fig. 10) and therefore we cannot compare the pressures of the hot phase between the two approaches in case of peak driving. If there is a random component (run M50-n$_3$), then the pressures of the hot phase are the same for thermal energy injection and combined model. The reason is that, in case of thermal energy injection, SNe which explode in dense gas cool on short time scales and do not contribute to the hot gas phase.

Furthermore, both mixed and peak driving show a slightly reduced pressure of the warm phase when the combined scheme is applied. For the mixed driving case (run M50-n$_3$), this brings the warm and the cold phase into pressure equilibrium. For the peak driving case (run P-C-n$_3$), the pressure of the warm phase appears to be smaller than the pressure of the cold phase. This is an artefact. Since the young SN bubbles themselves contribute significantly to the warm phase (because we set the temperature within the injection region to 10^4 K when momentum is injected), the warm phase is not formed self-consistently in this simulation. However, the thermal energy injected in this way is between $1-9$ % $E_{\rm SN}$, with the majority of SNe lying in the range $1-5$ %, in very good agreement with Kim & Ostriker (2014), Martizzi et al. (2014) and Walch & Naab (2014).

Volume Filling Fractions: The VFFs of the cold gas increase when using the momentum input scheme, which is more efficient in dispersing dense gas than the thermal injection method. As described above, the hot phase is missing or negligible when modelling SNe with momentum injection.

HI and H_α velocity dispersion: The derived one dimensional HI velocity dispersion is slightly lower for the combined model. The H_α emission is sensitive to the actual physical state of the warm component. Setting an upper temperature value of 10^4 K within the SN remnants

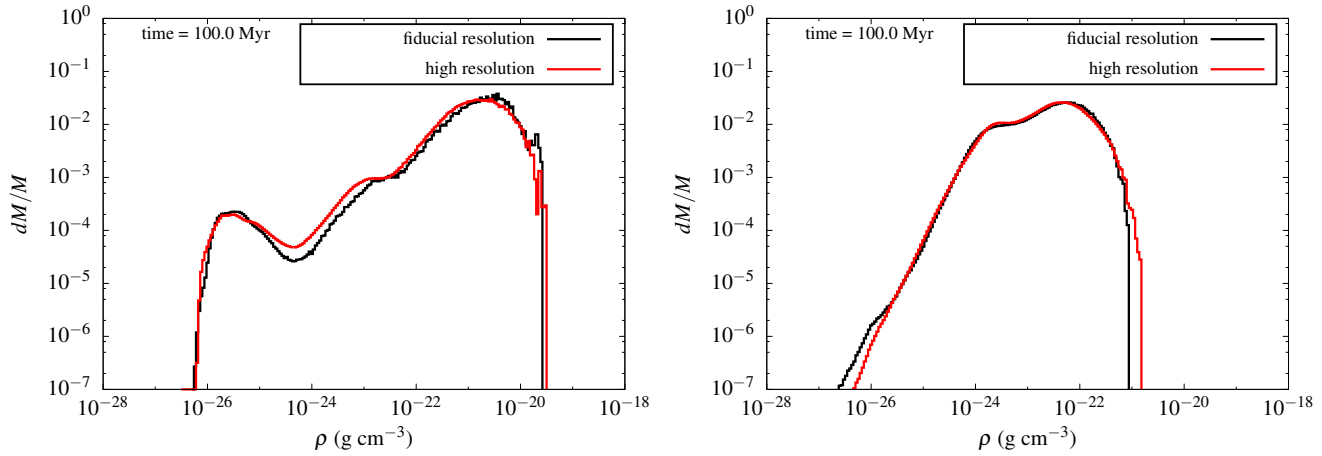

Figure 12. Mass-weighted density PDFs for random (left column, runs R-n$_3$ and R-HR-n$_3$) and peak driving (right column, runs P-n$_3$ and P-HR-n$_3$) for simulations with $\Delta x = 2$ pc (fiducial resolution) or 1 pc (higher resolution), and our fiducial parameters $n_\mathrm{i} = 3\,\mathrm{cm}^{-3}$ and $\dot{N}_\mathrm{SN,KS}$.

strongly influences the derived H$_\alpha$ velocity dispersion. We do not recommend to trust the H$_\alpha$ velocity dispersion if the thermal state of the gas within the injection region has not been derived in a self-consistent way.

3.8 Higher resolution

As an alternative one may avoid having $T_\mathrm{i,SN} < 10^6$ K in the SN injection region by going to a higher numerical resolution. We run two additional simulations with resolution $\Delta x = 1$ pc with pure peak and random driving (with pure thermal injection) for our fiducial setup ($n_\mathrm{i} = 3\,\mathrm{cm}^{-3}$ and $\dot{N}_\mathrm{SN,KS}$). For peak driving, this increase of a factor of two in resolution shifts the fraction of SNe having an estimated $T_\mathrm{i,SN} > 10^6$ K from 65% to 96%, while for random driving this value is close to unity in both cases. As shown in Figure A2, simulations with different resolutions do not display any substantial discrepancy in their temporal evolution.

In Figure 12 we compare the mass-weighted density PDFs for the fiducial and high resolution simulations for random (left panel) and peak driving (right panel). We plot the mass-weighted PDF as this emphasises differences in the high density regime, which is most critical. The density PDFs also show good convergence between fiducial and higher resolution, with an increase in density of rather less than a factor of two.

Kim & Ostriker (2014) show that the conditions $R_\mathrm{ST} > 3\,\Delta x$ and $R_\mathrm{ST} > 3\,R_\mathrm{inj}$ should be satisfied in order to recover a final momentum close to the values retrieved from their high resolution, sub-pc simulations. Combining these criteria and having assumed $R_\mathrm{inj} \geqslant 4\,\Delta x$ (eq. 3), their requirements can be translated into $R_\mathrm{ST} > 12\,\Delta x$. This slightly differs from our criterion, where $R_\mathrm{ST} \geqslant R_\mathrm{inj} > 3\,\Delta x$. From eq. (6) (but see also section 3.7) $R_\mathrm{ST} \approx 30.6\,n^{-0.4}$ pc. Therefore one can show that the critical density of the injection region (ambient medium) below which a SN is considered to be resolved is $n_\mathrm{crit} \approx 2\,\mathrm{cm}^{-3}$ from the Kim & Ostriker (2014) criteria and $n_\mathrm{crit} \approx 59\,\mathrm{cm}^{-3}$ from ours at our fiducial resolution of 2 pc. For $\Delta x = 1$ pc, $n_\mathrm{crit} \approx 10\,\mathrm{cm}^{-3}$ from Kim & Ostriker (2014) and $n_\mathrm{crit} \approx 330\,\mathrm{cm}^{-3}$ for us. For an initial density of $3\,\mathrm{cm}^{-3}$, the highest densities reached are $n \sim 100 - 500\,\mathrm{cm}^{-3}$ (see Fig. 12, right panel) and, hence, only a fraction of SNe in the high resolution run can be considered to be resolved. At fiducial resolution both ours and Kim & Ostriker (2014) conditions reveal that all of the SNe are not resolved (see also left panel of Fig. 10). Therefore, simulations with peak driving and thermal injection with initial density $n_\mathrm{i} \geqslant 3\,\mathrm{cm}^{-3}$ suffer from an underestimate of the momentum input by SNe and hence should be considered representative of a lower limit of the impact of peak SNe.

4 CONCLUSIONS

Summary: In this work, we perform 3D hydrodynamic simulations to study the SN-driven ISM in periodic volumes of size $(256\ \mathrm{pc})^3$. We include radiative cooling and diffuse heating, shielding from dust, and molecular gas (self-)shielding, as well as a chemical network to follow HI, HII, H_2, CO and CII. We study media with different mean gas densities, $n_\mathrm{i} = 0.5,\ 1,\ 3,\ 10,$ and $30\ \mathrm{cm}^{-3}$, which, integrated over the box side, correspond to surface densities of $\Sigma_\mathrm{gas} \approx 4,\ 8,\ 24,\ 81,$ and $243\ \mathrm{M}_\odot\mathrm{pc}^{-2}$. After an initial phase of turbulent stirring at root-mean-square velocity of $10\,\mathrm{km\,s}^{-1}$ for one crossing time (25 Myr), we switch to supernova (SN) driving and follow the simulations for more than three additional crossing times.

The SN rates are constant for each simulation, but change with the mean box density according to the Kennicutt-Schmidt relation. We additionally perform models with a factor of two higher and lower SN rates. We explore the impact of the placement of the SNe relative to the dense gas. We distinguish between random positions (random driving), positioning on local density peaks (peak driving), and a mixture of the two (mixed driving). The different SN placements should reflect that SNe could explode (i) mostly in their birthplaces, where they might be deeply embedded (peak driving); (ii) preferentially in low density environments (random driving). Random driving provides a simple way to introduce SNe in evolved, low

density environments without including all the necessary extra physics (wind and ionisation feedback from massive stars; clustering of massive stars; runaway stars) acting in between the point of star formation and the SN explosion. For mixed driving, we perform a set of simulations where we explore different ratios of peak to random driving using the fiducial setup ($n_{\rm i} = 3\,{\rm cm}^{-3}$ and $\dot{N}_{\rm SN,KS}$).

Random driving at different supernova rates: In the case of random driving, most of the mass is in cold, dense atomic and molecular hydrogen, whereas most of the volume is filled with hot, rarefied gas. The ISM is out of pressure equilibrium in all simulations apart from two cases with lowest density and lowest SN rate. The synthetically observed 1D velocity dispersions are $\sim 5-7$ $\mathrm{km\,s^{-1}}$ in HI and $\sim 17-25$ $\mathrm{km\,s^{-1}}$ in H_α. Increasing the SN rate by a factor of two leads to an increase in the mean gas pressure of the different phases (cold, warm, hot medium), a small increase in the velocity dispersion ($\sim$ few $\mathrm{km\,s^{-1}}$), and higher HI mass fractions, while the H_2 mass fractions decrease. However, the volume is always completely filled with hot gas, unless we consider low densities ($n_{\rm i} \leqslant 1$ $\mathrm{cm^{-3}}$) and SN rates of $\dot{N}_{\rm SN} \lesssim 2$ $\mathrm{Myr^{-1}}$. We attribute this behaviour to a thermal runaway process (see section 3.3), which occurs at high pressures, where only the cold branch of the equilibrium cooling curve can be reached, and no two-phase medium can form. In our case, though, the pressures are artificially determined. The boxes are not allowed to reach hydrostatic equilibrium to a larger galactic potential, so the SNe continuously feed energy into the high-pressure, hot medium. Thus, they can push almost all of the gas mass into small, molecular clumps that quickly form molecular hydrogen.

Peak and mixed driving: For peak instead of random driving, the ISM has a completely different structure. It is dominated by a filamentary distribution of warm gas (mostly HI), with little to no hot gas present. SNe that explode in dense gas also disperse the cold medium, and therefore the mass fraction of molecular hydrogen is small. The absence of hot gas (volume filling fraction VFF $\ll 50\%$) is due to the low heating efficiency and strong cooling of the SNe, which interact with dense gas. However, due to our limited resolution, we note that the impact of peak SNe is probably underestimated in high density regions (for $n > 1-60\,\mathrm{cm^{-3}}$ with fiducial and $n > 10-300\,\mathrm{cm^{-3}}$ with high resolution). In these cases, one should anyway expand the model to include other important physical conditions and processes, such as stellar clustering, stellar winds, and ionising radiation, and non-constant SN rate are critical ingredients, that shape the ISM and have to be taken into account.

For the setup with $n_{\rm i} = 3$ $\mathrm{cm^{-3}}$ and $\dot{N}_{\rm SN,KS}$, we vary the fraction of peak driving to random driving to explore the effect of a mixed SN placement at different fractions $f_{\rm peak}$. A relatively sharp transition between the two regimes (peak and random) occurs when $\sim$50% of the SN are located within density peaks. As $f_{\rm peak}$ increases, the mass fraction in H_2 drops, and the VFF of the warm and cold gas decreases. Interestingly, we find that the pressure of the hot phase as well as the velocity dispersion in H_α increase with increasing peak fraction ($H_\alpha \sim 50$ $\mathrm{km\,s^{-1}}$ for 100% peak driving). This behaviour can be attributed to the younger age of the SN remnants that contribute to these quantities.

Combined energy and momentum input: In low density gas, the SNe are well resolved and we model them with thermal energy input. Explosions within high density regions are eventually unresolved and would be subject to strong radiative (over-)cooling. Therefore, we introduce a new model, which combines thermal energy input for resolved SNe and momentum input for unresolved SNe. The momentum input at the end of the Sedov-Taylor phase is calculated using the relations derived in Blondin et al. (1998). We put the model to work in two of the simulations (peak driving and mixed driving at $f_{\rm peak} = 50\%$). We find that the momentum input model fails to produce any hot gas because the shock speeds are too small to heat the medium to more than 10^4 K. Otherwise, the combined model gives similar results to the thermal energy injection model and is therefore a viable alternative to model SN in partly unresolved environments – with the limitation that the temperature structure of the gas is no longer self-consistent.

Clumpy H_2 in gas-rich discs: When thermal runaway sets in, hot gas at high pressure pushes the gas into small and dense clouds, leading to a fast and efficient conversion from HI to H_2. Warm gas directly cools towards the cold branch of the equilibrium curve and, similar to the case of a high far-UV interstellar radiation field, a bi-stable equilibrium between the cold and warm phases does not exist anymore. We speculate that the molecular-dominated, very clumpy structure of the ISM in simulations with a high gas surface density $\Sigma_{\rm gas} \gtrsim 100$ $\mathrm{M_\odot\ pc^{-2}}$ could be a reasonable representation of systems with high gas surface densities and very high mid-plane pressures like ULIRGs (Downes & Solomon 1998, but see also Rosolowsky & Blitz 2005) or normal star forming galaxies at high redshift (Genzel et al. 2010) that have high gas fractions and SFRs (e.g. Tacconi et al. 2010, 2013). Their mid-plane pressures are three to four orders of magnitudes higher than for the Milky Way (Bowyer et al. 1995; Berghöfer et al. 1998; Jenkins & Tripp 2011) and plausibly reach values of $P/k_{\rm B} \sim 10^{6-7}$ $\mathrm{K\,cm^{-3}}$ for surface densities of 100 $\mathrm{M_\odot\ pc^{-2}}$ and above (Swinbank et al. 2011), very similar to our models for $n_{\rm i} = 10$ or $30\,\mathrm{cm^{-3}}$ with random driving. Such high mid-plane pressure forces all the gas onto the cold branch of the equilibrium curve, so that it reaches densities that allow quick conversion from atomic to molecular gas. Thus, in high pressure, gas rich environments, the sizes and masses of the collapsing and H_2 forming structures could be regulated by supernova feedback. Our simulations show that the mass budget of the ISM can be dominated by molecular gas while, at the same time, this molecular gas is still found in small dense clumps with low filling factor surrounded by hot rarefied gas, rather than being evenly distributed. However, this picture needs to be refined with simulations of stratified, high-surface density discs (similar to Shetty & Ostriker 2012) and a more self-consistent treatment of star formation to address the issue of self-regulation in gas-rich environments. On the other hand, for low $\Sigma_{\rm gas} \sim 5$ $\mathrm{M_\odot\ pc^{-2}}$, where the ISM has reasonable pressures and VFFs, we find too little molec-

ular gas. Here we are probably missing the aid of self-gravity.

LIMITATIONS OF THE MODEL: For peak driving, the limited resolution employed raises concerns about the effectiveness of density peak SNe. Recent results from Kim & Ostriker (2014) suggest that our models with pure thermal injection should be considered to be lower limits on the impact of peak driving on the ISM. For random SNe, in particular for intermediate $\Sigma_{\rm gas} \sim 10 - 100$ M$_\odot$ pc^{-2}, the creation of high pressure, high VFF, hot gas in the random driving case is overestimated due to our choice of periodic boundary conditions in all three dimensions. In a stratified disc, these high pressures would power a galactic fountain or outflow, lowering the ambient pressure in the mid-plane to the hydrostatic equilibrium value within a crossing time (few dozens of Myr) of a scale height for the hot gas. Other key physical ingredients, such as ionising radiation, stellar winds, and stellar clustering, etc. could also play a crucial role in determining the state of the multi-phase ISM. For these reasons, the employment of the simplified setup presented here does not allow us to draw any quantitative conclusions. However, this kind of study clearly shows the qualitative consequences of each model.

5 ACKNOWLEDGEMENTS

We thank an anonymous referee for comments and suggestions that improved the clarity of this work. We also thank A. Pardi and A. Bubel for pointing out some minor errors in an earlier version of the paper. We thank A. Ballone and A. Caldú-Primo for stimulating discussions. The authors acknowledge the Deutsche Forschungsgemeinschaft (DFG) for funding through the SPP 1573 "The Physics of the Interstellar Medium". S. Walch acknowledges funding by the Bonn-Cologne-Graduate School. M-M. Mac Low acknowledges support from NSF grant AST11-09395 and the Alexander von Humboldt-Stiftung. R. S. Klessen and S. Glover acknowledge support from the DFG via SFB 881 "The Milky Way System" (sub-projects B1, B2 and B8). R. S. Klessen furthermore acknowledges support from the European Research Council under the European Communitys Seventh Framework Programme (FP7/2007-2013) via the ERC Advanced Grant STARLIGHT (project number 339177). R. Wünsch acknowledges support by project P209/12/1795 of the Czech Science Foundation and by project RVO: 67985815. T. Peters acknowledges financial support through a Forschungskredit of the University of Zürich, grant no. FK-13-112. A. Gatto visited the AMNH with support from a Kade Fellowship during completion of this work. The software used in this work was in part developed by the DOE NNSA-ASC OASCR Flash Center at the University of Chicago. We thank C. Karch for the program package FY and M. Turk and the YT community for the YT project (Turk et al. 2011). The authors gratefully acknowledge the Gauss Centre for Supercomputing for funding this project by providing support and high-performance computing time on SuperMUC at the Leibniz Supercomputing Centre (LRZ). Additional simulations have been performed on the Odin and Hydra clusters at the Rechenzentrum Garching (RZG).

REFERENCES

Aggarwal K. M., 1983, MNRAS, 202, 15P
Anderson H., Ballance C. P., Badnell N. R., Summers H. P., 2000, Journal of Physics B Atomic Molecular Physics, 33, 1255
Anderson H., Ballance C. P., Badnell N. R., Summers H. P., 2002, Journal of Physics B Atomic Molecular Physics, 35, 1613
Balsara D. S., Kim J., Mac Low M.-M., Mathews G. J., 2004, ApJ, 617, 339
Banerjee R., Vázquez-Semadeni E., Hennebelle P., Klessen R. S., 2009, MNRAS, 398, 1082
Berghöfer T. W., Bowyer S., Lieu R., Knude J., 1998, ApJ, 500, 838
Blaauw A., 1961, Bulletin of the Astronomical Institutes of the Netherlands, 15, 265
Blondin J. M., Wright E. B., Borkowski K. J., Reynolds S. P., 1998, ApJ, 500, 342
Bouchut F., Klingenberg C., Waagan K., 2007, Numer. Math., 108, 7
Bouchut F., Klingenberg C., Waagan K., 2010, Numer. Math., 115, 647
Bowyer S., Lieu R., Sidher S. D., Lampton M., Knude J., 1995, Nature, 375, 212
Brighenti F., D'Ercole A., 1994, MNRAS, 270, 65
Caldú-Primo A., Schruba A., Walter F., Leroy A., Sandstrom K., de Blok W. J. G., Ianjamasimanana R., Mogotsi K. M., 2013, AJ, 146, 150
Cioffi D. F., McKee C. F., Bertschinger E., 1988, ApJ, 334, 252
Clark P. C., Glover S. C. O., Klessen R. S., 2012, MNRAS, 420, 745
Cox D. P., Smith B. W., 1974, ApJL, 189, L105
Creasey P., Theuns T., Bower R. G., Lacey C. G., 2011, MNRAS, 415, 3706
Dale J. E., Ngoumou J., Ercolano B., Bonnell I. A., 2014, MNRAS, 442, 694
de Avillez M. A., Breitschwerdt D., 2004, A&A, 425, 899
de Avillez M. A., Breitschwerdt D., 2007, ApJL, 665, L35
Dib S., Bell E., Burkert A., 2006, ApJ, 638, 797
Dong R., Draine B. T., 2011, ApJ, 727, 35
Downes D., Solomon P. M., 1998, ApJ, 507, 615
Draine B. T., 1978, ApJS, 36, 595
Draine B. T., 2011, Physics of the Interstellar and Intergalactic Medium
Dubey A., Antypas K., Calder A. C., Daley C., Fryxell B., Gallagher J. B., Lamb D. Q., Lee D., Olson K., Reid L. B., Rich P., Ricker P. M., Riley K. M., Rosner R., Siegel A., Taylor N. T., Weide K., Timmes F. X., Vladimirova N., ZuHone J., 2013, International J. High Perf. Comput. Appl., 551, L105
Dubey A., Fisher R., Graziani C., Jordan IV G. C., Lamb D. Q., Reid L. B., Rich P., Sheeler D., Townsley D., Weide K., 2008, in Pogorelov N. V., Audit E., Zank G. P., eds, Numerical Modeling of Space Plasma Flows Vol. 385 of Astronomical Society of the Pacific Conference Series, Challenges of Extreme Computing using the FLASH code. p. 145
Eldridge J. J., Langer N., Tout C. A., 2011, MNRAS, 414, 3501
Elmegreen B. G., Lada C. J., 1977, ApJ, 214, 725

Elmegreen B. G., Scalo J., 2004, ARA&A, 42, 211
Eswaran V., Pope S., 1988, Computers and Fluids, 16, 257
Ferrière K. M., 2001, Rev. Mod. Phys., 73, 1031
Fryxell B., Olson K., Ricker P., Timmes F. X., Zingale M., Lamb D. Q., MacNeice P., Rosner R., Truran J. W., Tufo H., 2000, ApJS, 131, 273
Fujii M. S., Portegies Zwart S., 2011, Science, 334, 1380
Fukui Y., Moriguchi Y., Tamura K., Yamamoto H., Tawara Y., Mizuno N., Onishi T., Mizuno A., Uchiyama Y., Hiraga J., Takahashi T., Yamashita K., Ikeuchi S., 2003, PASJ, 55, L61
Gatto A., Fraternali F., Read J. I., Marinacci F., Lux H., Walch S., 2013, MNRAS, 433, 2749
Gent F. A., Shukurov A., Fletcher A., Sarson G. R., Mantere M. J., 2013, MNRAS, 432, 1396
Genzel R., Tacconi L. J., Gracia-Carpio J., et al., 2010, MNRAS, 407, 2091
Gies D. R., 1987, ApJS, 64, 545
Gies D. R., Bolton C. T., 1986, ApJS, 61, 419
Glover S. C. O., Clark P. C., 2012, MNRAS, 421, 116
Glover S. C. O., Federrath C., Mac Low M.-M., Klessen R. S., 2010, MNRAS, 404, 2
Glover S. C. O., Mac Low M.-M., 2007a, ApJS, 169, 239
Glover S. C. O., Mac Low M.-M., 2007b, ApJ, 659, 1317
Gnat O., Ferland G. J., 2012, ApJS, 199, 20
Goodman A. A., Barranco J. A., Wilner D. J., Heyer M. H., 1998, ApJ, 504, 223
Gritschneder M., Naab T., Walch S., Burkert A., Heitsch F., 2009, ApJL, 694, L26
Habing H. J., 1968, Bulletin of the Astronomical Institutes of the Netherlands, 19, 421
Heiles C., Troland T. H., 2003, ApJ, 586, 1067
Heitsch F., Naab T., Walch S., 2011, MNRAS, 415, 271
Heitsch F., Slyz A. D., Devriendt J. E. G., Hartmann L. W., Burkert A., 2006, ApJ, 648, 1052
Hennebelle P., Iffrig O., 2014, A&A, 570, A81
Hewitt J. W., Yusef-Zadeh F., 2009, ApJL, 694, L16
Hill A. S., Joung M. R., Mac Low M.-M., Benjamin R. A., Haffner L. M., Klingenberg C., Waagan K., 2012, ApJ, 750, 104
Hopkins P. F., Kereš D., Oñorbe J., Faucher-Giguère C.-A., Quataert E., Murray N., Bullock J. S., 2014, MNRAS, 445, 581
Iffrig O., Hennebelle P., 2014, ArXiv e-prints, arXiv:1410.7972
Jenkins E. B., Tripp T. M., 2011, ApJ, 734, 65
Joung M. K. R., Mac Low M.-M., 2006, ApJ, 653, 1266
Joung M. R., Mac Low M.-M., Bryan G. L., 2009, ApJ, 704, 137
Kalberla P. M. W., Dedes L., 2008, A&A, 487, 951
Kalberla P. M. W., Kerp J., 2009, ARA&A, 47, 27
Keller B. W., Wadsley J., Benincasa S. M., Couchman H. M. P., 2014, ArXiv e-prints, arXiv:1405.2625
Kennicutt Jr. R. C., 1998, ApJ, 498, 541
Kim C.-G., Kim W.-T., Ostriker E. C., 2011, ApJ, 743, 25
Kim C.-G., Ostriker E. C., 2014, ArXiv e-prints, arXiv:1410.1537
Kim C.-G., Ostriker E. C., Kim W.-T., 2013, ApJ, 776, 1
Kim J., 2004, Journal of Korean Astronomical Society, 37, 237
Kim J.-h., Krumholz M. R., Wise J. H., Turk M. J., Goldbaum N. J., Abel T., 2013, ApJ, 779, 8
Klessen R. S., Hennebelle P., 2010, A&A, 520, A17
Krause M., Fierlinger K., Diehl R., Burkert A., Voss R., Ziegler U., 2013, A&A, 550, A49
Kritsuk A. G., Norman M. L., 2002, ApJL, 569, L127
Lada C. J., Lada E. A., 2003, ARA&A, 41, 57
Larson R. B., 1981, MNRAS, 194, 809
Mac Low M.-M., Balsara D. S., Kim J., de Avillez M. A., 2005, ApJ, 626, 864
Mac Low M.-M., Klessen R. S., 2004, Reviews of Modern Physics, 76, 125
Mac Low M.-M., McCray R., 1988, ApJ, 324, 776
Martizzi D., Faucher-Giguère C.-A., Quataert E., 2014, ArXiv e-prints, arXiv:1409.4425
McCray R., Kafatos M., 1987, ApJ, 317, 190
McKee C. F., Ostriker J. P., 1977, ApJ, 218, 148
Mestel L., Spitzer Jr. L., 1956, MNRAS, 116, 503
Micic M., Glover S. C. O., Banerjee R., Klessen R. S., 2013, MNRAS, 432, 626
Norman C. A., Ferrara A., 1996, ApJ, 467, 280
Ostriker E. C., McKee C. F., Leroy A. K., 2010, ApJ, 721, 975
Péquignot D., Tsamis Y. G., 2005, A&A, 430, 187
Perets H. B., Šubr L., 2012, ApJ, 751, 133
Petric A. O., Rupen M. P., 2007, AJ, 134, 1952
Pflamm-Altenburg J., Kroupa P., 2010, MNRAS, 404, 1564
Portegies Zwart S. F., 2000, ApJ, 544, 437
Raymond J. C., Cox D. P., Smith B. W., 1976, ApJ, 204, 290
Rogers H., Pittard J. M., 2013, MNRAS, 431, 1337
Rohlfs K., Wilson T. L., 1996, Tools of Radio Astronomy
Rosolowsky E., Blitz L., 2005, ApJ, 623, 826
Salpeter E. E., 1955, ApJ, 121, 161
Saury E., Miville-Deschênes M.-A., Hennebelle P., Audit E., Schmidt W., 2014, A&A, 567, A16
Scannapieco E., Gray W. J., Pan L., 2012, ApJ, 746, 57
Schmidt M., 1959, ApJ, 129, 243
Sellwood J. A., Balbus S. A., 1999, ApJ, 511, 660
Sembach K. R., Howk J. C., Ryans R. S. I., Keenan F. P., 2000, ApJ, 528, 310
Sharma P., Roy A., Nath B. B., Shchekinov Y., 2014, MNRAS, 443, 3463
Shetty R., Ostriker E. C., 2012, ApJ, 754, 2
Shull J. M., Saken J. M., 1995, ApJ, 444, 663
Simpson C. M., Bryan G. L., Hummels C., Ostriker J. P., 2014, ArXiv e-prints, arXiv:1410.3822
Slyz A. D., Devriendt J. E. G., Bryan G., Silk J., 2005, MNRAS, 356, 737
Stinson G., Seth A., Katz N., Wadsley J., Governato F., Quinn T., 2006, MNRAS, 373, 1074
Stone R. C., 1991, AJ, 102, 333
Swinbank A. M., Papadopoulos P. P., Cox P., Krips M., Ivison R. J., Smail I., Thomson A. P., Neri R., Richard J., Ebeling H., 2011, ApJ, 742, 11
Tacconi L. J., Genzel R., Neri R., Cox P., Cooper M. C., Shapiro K., Bolatto A., et al., 2010, Nature, 463, 781
Tacconi L. J., Neri R., Genzel R., Combes F., Bolatto A., Cooper M. C., Wuyts S., Bournaud F., Burkert A., Comerford J., et al., 2013, ApJ, 768, 74
Tamburro D., Rix H.-W., Leroy A. K., Mac Low M.-M., Walter F., Kennicutt R. C., Brinks E., de Blok W. J. G., 2009, AJ, 137, 4424

Tammann G. A., Loeffler W., Schroeder A., 1994, ApJS, 92, 487
Tenorio-Tagle G., Bodenheimer P., 1988, ARA&A, 26, 145
Tenorio-Tagle G., Bodenheimer P., Franco J., Rozyczka M., 1990, MNRAS, 244, 563
Tenorio-Tagle G., Rozyczka M., Franco J., Bodenheimer P., 1991, MNRAS, 251, 318
Thacker R. J., Couchman H. M. P., 2000, ApJ, 545, 728
Turk M. J., Smith B. D., Oishi J. S., Skory S., Skillman S. W., Abel T., Norman M. L., 2011, ApJS, 192, 9
Vázquez-Semadeni E., Gazol A., Scalo J., 2000, ApJ, 540, 271
Vázquez-Semadeni E., Ryu D., Passot T., González R. F., Gazol A., 2006, ApJ, 643, 245
Waagan K., 2009, Journal of Computational Physics, 228, 8609
Wada K., Meurer G., Norman C. A., 2002, ApJ, 577, 197
Walch S., Whitworth A. P., Bisbas T. G., Wünsch R., Hubber D. A., 2013, MNRAS, 435, 917
Walch S., Wünsch R., Burkert A., Glover S., Whitworth A., 2011, ApJ, 733, 47
Walch S. K., Girichidis P., Naab T., Gatto A., Glover S. C. O., Wünsch R., Klessen R. S., Clark P. C., Peters T., Baczynski C., 2014, ArXiv e-prints, arXiv:1412.2749
Walch S. K., Naab T., 2014, ArXiv e-prints, arXiv:1410.0011
Walch S. K., Whitworth A. P., Bisbas T., Wünsch R., Hubber D., 2012, MNRAS, 427, 625
Wolfire M. G., Hollenbach D., McKee C. F., Tielens A. G. G. M., Bakes E. L. O., 1995, ApJ, 443, 152

APPENDIX A: TEMPORAL EVOLUTION VS. TIME AVERAGE

In this section we show the differences between the analysed quantities averaged over the last 5 Myr of each simulation and their full temporal evolution. Generally, due to our choice of stopping the simulations once a chemodynamical equilibrium is reached, different runs have different final times. This already introduces uncertainty when comparing different simulations with quantities averaged over the last 5 Myr.

Figure A1 shows the evolution of mass fractions, VFFs, pressures, and velocity dispersions for the fiducial setup with pure random (left column) and pure peak driving (right column). For random driving the evolution of the quantities is smooth and the time average fairly portrays the global trend. On the other hand, for peak driving this is not true anymore. Highly time-varying H_2 mass fraction, σ_{H_α}, hot gas pressure, and VFF cause the time average to be not completely representative of the temporal trend. This behaviour is also important when comparing simulations with same driving mode, as shown in Figure A2 for peak driving with fiducial (left column) and high resolution (right column). This effect, although not significant, should be taken into account when comparing simulations.

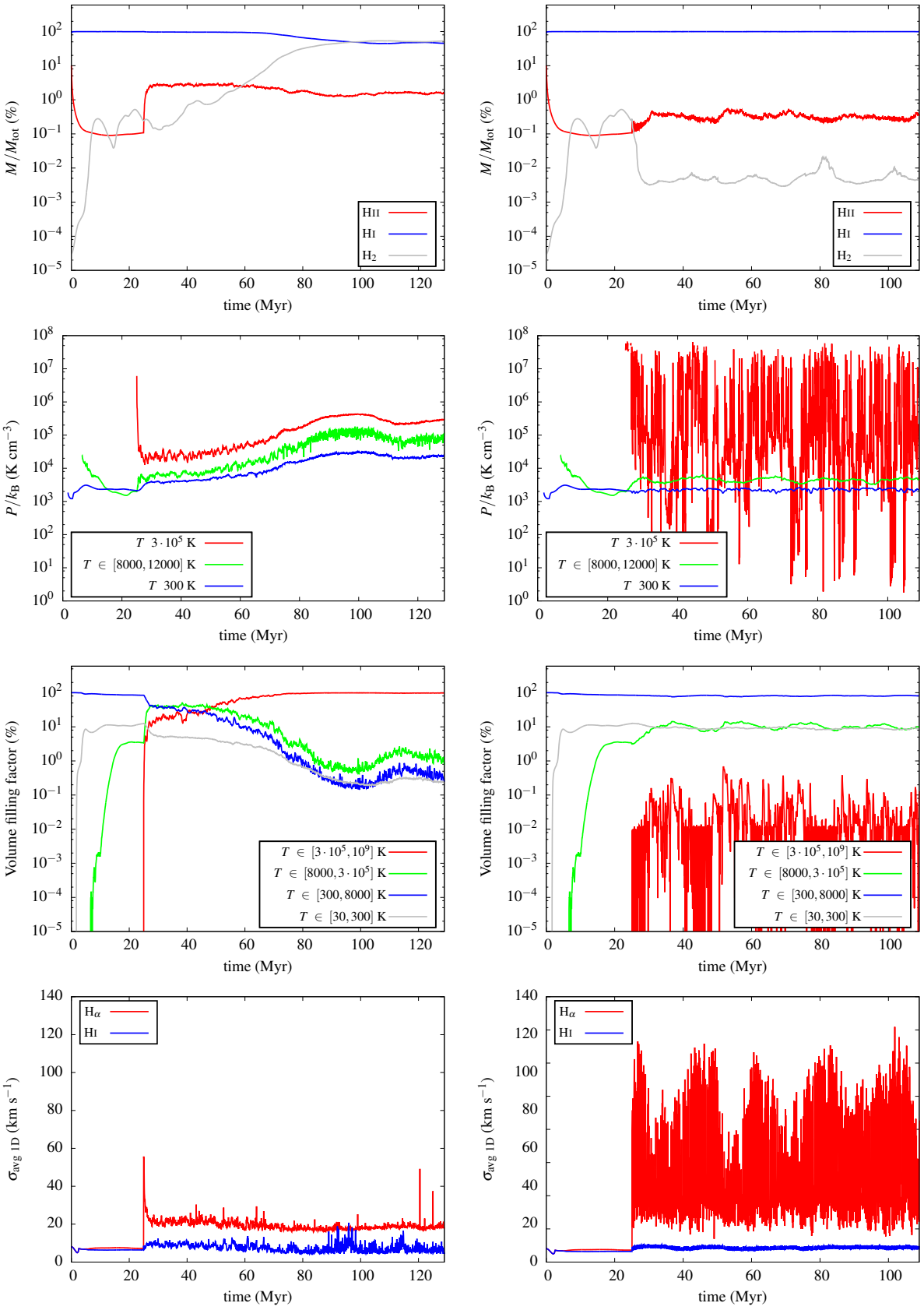

Figure A1. Evolution of mass fractions, pressures, VFFs and velocity dispersions for $n_{\rm i} = 3\,{\rm cm}^{-3}$ and $\dot{N}_{\rm SN,KS}$ with random (left column) and peak driving (right column).

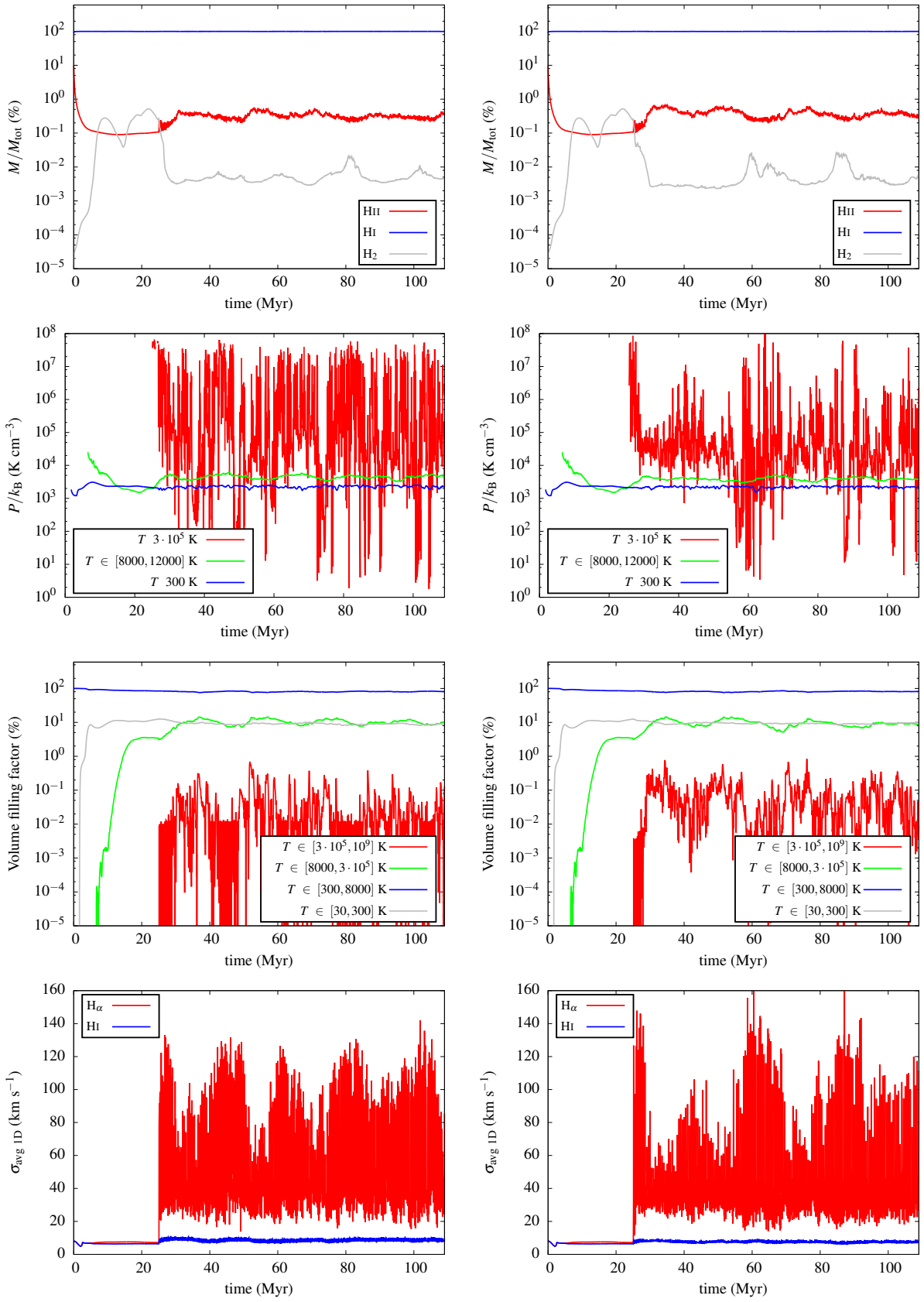

Figure A2. Evolution of mass fractions, pressures, VFFs and velocity dispersions for $n_{\rm i} = 3\,{\rm cm}^{-3}$ and $\dot{N}_{\rm SN,KS}$ with peak driving for the fiducial resolution of $\Delta x = 2$ pc (left column) and for higher resolution of $\Delta x = 1$ pc (right column).